

ALMA MATER STUDIORUM · UNIVERSITY OF BOLOGNA

Department of Physics and Astronomy
Master Degree in Physics

**Operando X-ray absorption spectroscopy studies
of Fe and Co based catalyst on WO₃/BiVO₄
photoanodes for water splitting**

Supervisor:
Prof. Federico Boscherini

Submitted by:
Alessia Bardazzi

Co-supervisor:
Dott. Raffaello Mazzaro

**Sessione VI
Academic Year 2021/2022**

Abstract

The goal of this thesis is to experimentally study the local atomic and electronic structure of two compounds used as co-catalysts of photoelectrochemical reactions using X-ray absorption spectroscopy (XAS) with synchrotron radiation. Specifically, CoFe-prussian blue and amorphous CoFe-oxide layers deposited on $WO_3/BiVO_4$ were studied before, during and after photoelectrocatalysis. Firstly, *ex-situ* XAS at the Fe and Co K-edges were performed in order to understand the initial local structure around these cations. Then, the samples spectroscopical features were investigated by employing a specifically designed photoelectrochemical cell, and *operando* measurements were performed under the application of a bias potential and illumination in order to reproduce the operating conditions. In absence of light excitation, we investigated the bias-dependence of the XAS spectrum on Co-K edge for both catalysts, observing that the cocatalyst oxidizes while in the PEC cell under bias. When the electrolyte is removed, it tends to revert to the initial state. Successively, to see the effect of light, a second *operando* measurement were performed illuminating the samples (while in PEC with electrolyte) in two different methods: by illuminating constantly and intermittently. We found that illuminating the sample produces a slight modification in the absorption spectra, which was further investigated by FEXRAV (fixed energy X-ray absorption voltammetry). This last technique was performed to map better the oxidation states of the samples in the applied potential window, finding out that *CoFe - PB* and *CoFeOx* have different behaviour. In fact, for *CoFe - PB* it takes an higher voltage in the dark than in the light to start the oxidation process whereas for *CoFeOx* the opposite behavior is found. A preliminary interpretation is that this is due to the different recombination processes of electrons between the co-catalyst and $BiVO_4$.

Contents

1	Introduction	1
2	X-ray Absorption Spectroscopy	3
2.1	X-Ray Absorption Spectroscopy	4
2.2	Experimental methods	6
2.3	Theoretical background	7
2.4	Extended X-ray Absorption Fine Structure: EXAFS	9
2.5	X-ray Absorption Near Edge Structure (XANES)	12
2.6	Fluorescence Spectroscopy	15
3	Photoelectrocatalysis	16
3.1	Principle of Photoelectrocatalysis	17
3.2	Charge Carriers and Doping	21
3.3	Space Charges and Band Bending	22
3.4	The Band Diagram	23
3.5	Applying A Bias Potential	24
3.6	pH Dependence of The Band Edges	25
3.7	The Photoelectrochemical Cell Under Operating Conditions	25
3.8	Photocurrent–Voltage Characteristics	27
3.9	Semiconducting Photoelectrode Materials	27
3.9.1	Photoanode: Bismuth vanadate on tungsten trioxide	29
3.10	Catalyst: Mixed cobalt iron compounds	31
4	Experimental apparatus	35
4.1	X-ray source: European Synchrotron Radiation Facility	36
4.1.1	LISA (<i>Linea Italiana per la Spettroscopia di Assorbimento X</i>) beam- line	37
4.2	The photoelectrochemical cell	38
4.3	Potentiostat	39
4.4	Additional components	40
4.5	Data acquisition	40
5	Results and discussion	42
5.1	Description of the samples	42
5.1.1	$WO_3/BiVO_4/CoFe - PB$	43
5.1.2	$WO_3/BiVO_4/CoFeOx$	45

5.2	<i>Ex-situ</i> XAS investigation	45
5.3	<i>Operando</i> XAS investigation	48
5.4	FEXRAV: Fixed energy X-ray absorption voltammetry	52
6	Conclusions	56

List of Figures

2.1	Different types of interaction between X-rays and matter.	4
2.2	Spectra of an isolated atom, K-edge of Argon (left), and the fine structure of Germanium(right). [2]	5
2.3	Experimental set of a XAS experiment. The X-ray beam passes through a monochromator and a slit to select the wavelength. Then the X-ray is detected before and after traversing the sample.	6
2.4	Possible outcomes after a photon absorption. On the left it is shown the emission of a characteristic X-ray, whereas on the right there is the emission of an electron called Auger electron. This two outcomes are in competition and can not happen together.	7
2.5	Interaction between atoms that originates the fine structure. When an X-ray photon of high enough energy is absorbed by an atom A, a core electron is ejected from the atom. If the absorber atom A is not isolated, the photo-electron can be scattered by a neighbouring atom B. The total photo-electron wavefunction is now a superposition of the outgoing and the scattered waves.	9
2.6	Effect of Fourier transformation on EXAFS signal. On the left is displayed the EXAFS signal whereas on the right the Fourier transformation of the crystalline germanium at 77K [2].	11
2.7	Different Ti K-edge XANES produced by different Ti^{4+} coordination geometries [2].	13
2.8	Different compounds of Sulfur produce different Sulfur K-edge XANES spectra and shifted edges [2].	14
3.1	Illustration of a photoelectrochemical cell that consists of a semiconducting photoanode and a metal cathode. The corresponding energy diagram is shown in the right [3].	17
3.2	Photoelectrochemical device configurations for solar hydrogen production [12].	18
3.3	Different configuration of PEC cells for the evaluation of the photoanode activity under simulated sunlight [10].	20
3.4	Mott-Schottky plot for ZnO in the semiconductor-electrolyte, $7 \cdot 10^{-4} M K_3[Fe(CN)_6]$ [9].	22
3.5	Energy diagram for a PEC cell based on a n-type semiconductor and a metal counter electrode. [3].	23

3.6	Effect of applying a bias voltage V_A to an n-type semiconductor electrode. Any change in applied potential falls across the space charge layer, whereas V_H remains constant. In the picture on the left, a positive potential is applied to the semiconductor. The band bending can be reduced to zero When a sufficiently negative bias is applied [3].	24
3.7	Band diagram for a PEC cell based on an n-type semiconducting photoanode that is electrically connected to a metal counter electrode. Illumination raises the Fermi level and decreases the band bending. The Fermi level near the semiconductor/electrolyte interface, splits into quasi-Fermi levels for the electrons and holes [3].	26
3.8	On the left: Band positions for n-photoanode materials. On the right: Solar absorption of n-photoanodes materials [8].	29
3.9	FESEM micrographs of a) WO_3 , b) $WO_3/BiVO_4$. d) XRD pattern of the prepared photoanodes and reference patterns for WO_3 and $BiVO_4$ [23]. . .	30
3.10	Energy diagram of the $WO_3/BiVO_4$ heterojunction (at pH 7) and electron transport process [6].	30
3.11	Current potential (with respect to normal hydrogen electrode NHE scale) plots for (red line, a) planar $WO_3/BiVO_4$ heterojunction film, (blue line, b) planar WO_3 film, and (green line, c) planar $BiVO_4$ film illuminated with chopped white light ($100mW/cm^2$) in an aqueous solution of $0.5mol \cdot L^{-1}$ sodium sulfate (Na_2SO_4) [6].	31
3.12	a) Structure and b) unit cell of PB.	32
3.13	Comparison of the TA spectra of persistent photogenerated charges (recorded at 10 ms) in $CoFe - PB$ modified and unmodified $BiVO_4$ [14].	32
3.14	a) Processes in unmodified $WO_3/BiVO_4$, where we have the recombination competing with the water oxidation. b) Adding the catalyst $CoFePB$ the recombination current is suppressed enhancing the efficiency.	33
4.1	Simplified scheme of the setup for photoelectrochemical measurements. . . .	35
4.2	a) Satellite image of ESRF, <i>Earth data 2016 Google</i> . b) Scheme of the structure of a synchrotron. It includes a LINAC (Linear particle accelerator), a booster, a storage ring and beamlines.	36
4.3	General layout of the LISA beamline. The center of the first hutch (optics hutch OH) is about 28 m from the source, the first experimental hutch ($EH1$) is at 37 m and the second experimental hutch ($EH2$) is at 49 m. [18].	38
4.4	3D sketch and pictures of the photoelectrochemical cell used for photoelectrochemical measurements. a) Cross section view. b) Complete picture of the cell from outside.	39
4.5	Simplified internal circuit of a potentiostat. OA is the operational amplifier that keep the voltage between the reference and the working electrode at the desired voltage.	39
4.6	a) View of the computers in the control room while the experiment was performing. b) Inside of the chamber with light ON and PEC cell.	40

4.7	Behaviour of light during a) the first <i>operando</i> measurement with light, keeping the light always ON or OFF, and b) the second <i>operando</i> measurement, with light ON for 10 s and then OFF 10 s with a delay of 1 s for every X-ray's energy.	41
5.1	FESEM micrograph of a) WO_3 , b) $WO_3/BiVO_4$ and c) $WO_3/BiVO_4/CoFe-PB$. d) XRD pattern of the built photoanodes and the reference patterns for WO_3 and $BiVO_4$ [23].	44
5.2	Linear sweep voltammetry under 1-sun equivalent illumination in acetate buffer solution (pH 5) of only $WO_3/BiVO_4$ (red line) and in presence of the co-catalyst a) $CoFePB$ (blue line); b) $CoFeOx$ (black line).	45
5.3	a) Fe K-edge and b) Co K-edge spectra performed on $CoFeOx$, black line, and $CoFe - PB$, red line. The spectra of $CoFeOx$, black line, was shifted on the y-axis by a value of 0.3 to show better both the spectra.	46
5.4	Co k-edge EXAFS spectra and its Fourier of $CoFe - PB$ a)-b) and $CoFeOx$ c)-d).	47
5.5	a) FT of Co k-edge EXAFS of $CoFe - PB$ (red line) and the reference one of $FeCo(CN)_6$ (blue line). b) Structure of molecule $FeCo(CN)_6$	48
5.6	a) Co k-edge XANES of $CoFe - PB$ while the sample was in the PEC cell with electrolyte solution borate buffer 0.5 M (pH9), biased at various voltages. The spectra taken before and after (black and pink lines) was taken <i>ex-situ</i> and shifted on the y-axis to show better the features of interest. b) Enlargement of the edge region to observe better the shift.	48
5.7	a) Co k-edge XANES of $CoFeOx$ while the sample was in the PEC cell with electrolyte solution borate buffer 0.5 M (pH9), biased at various voltages. The spectra taken before and after (black and pink lines) was taken <i>ex-situ</i> and shifted on the y-axis to show better the features of interest. b) Enlargement of the edge region to observe better the shift.	49
5.8	Comparison of Co K-edge XANES of $CoFe - PB$ a)-c) and $CoFeOx$ b)-d) while the sample was in the PEC cell with electrolyte solution borate buffer 0.5M (pH 9), biased at various V. The voltage 0.2 V (blue line) was used as reference and the difference between the spectra is always plotted as the purple line.	50
5.9	a) Comparison of Co k-edge XANES of $CoFe - PB$ in <i>operando</i> conditions and the reference spectra of CoCat. b) CoCat's structure [26].	50
5.10	Co K-edge XANES of $CoFe - PB$ while the sample was in the PEC cell with an electrolyte solution borate buffer 0.5 M (pH 9) and biased at various voltages with light OFF or ON. The light purple and brown line show the difference between the ON and OFF spectra at the same V.	51
5.11	Co k-edge XANES of a) $CoFe - PB$ and b) of $CoFeOx$ while the sample was in the PEC cell switching light OFF 10 s then ON for 10 s (with delay of 1 s) while the sample was immersed in an electrolyte solution borate buffer 0.5 M (pH 9) and biased at various voltages.	52

- 5.12 a) Co k-edge FEXRAV of $CoFe - PB$, with an applied voltage $[(-0.2) - (1.5)] V$ and energy fixed at $7722.5 eV$. In the graph is shown the μ (red line), the current (blue line), and the voltage (green line) as a function of time. b) Cyclic voltammetry of $CoFe - PB$ in the range $-0.2 V < V vs Ref < 1.5 V$. c) Co k-edge spectra of $CoFe - PB$ with a light purple line on $7722.5 eV$, the energy chosen to perform FEXRAV. 53
- 5.13 a) Co k-edge FEXRAV of $CoFeOx$, with an applied voltage $[(-0.2) - (1.5)] V$ and energy fixed at $7719.5 eV$. In the graph is shown the μ (red line), the current (blue line), and the voltage (green line) as a function of time. b) Cyclic voltammetry of $CoFeOx$ in the range $-0.2 V < V vs Ref < 1.5 V$. c) Co k-edge spectra of $CoFeOx$ with a light purple line on $7719.5 eV$, the energy chosen to perform FEXRAV. 54
- 5.14 PEC cell using $CoFeOx$ as cocatalyst a) in dark and b) illuminated. The cocatalyst is first reduced in dark and then, oxidized in light due to the quasi-Fermi level at more positive energy. 54
- 5.15 PEC cell using $CoFe - PB$ as cocatalyst a) in dark and b) illuminated. The cocatalyst is reduced in dark and then a second time in light due to the Fermi level at more negative energy in both cases and a small band bending. 55

Chapter 1

Introduction

Nowadays the world is facing a global energy crisis and environmental pollution problem due to the rapid population growth rate and revolution in industrialization. At the moment the most used energy sources are coming from nonrenewable fossil fuels. These reserves are running down rapidly and cause tremendous environmental damage with high carbon and toxic gas emission. Therefore the need for renewable energy sources has increased exponentially and is now imperative. Renewable energy sources include wind, hydropower, bioenergy, geothermal, and solar energy. Among these, the solar energy is booming as the most efficient source providing the Earth annually with 1.08×10^8 GW (which is 7000–8000 times annual global primary energy consumption) [1]. However it is still very difficult to reduce the cost of solar energy conversion processes and devices and to store solar fuel efficiently. To overcome this problem, renewable hydrogen production from solar water splitting by photocatalysis (PC) and photoelectrocatalysis (PEC) is studied more and more. This two processes exploit water splitting mechanism, by which hydrogen fuel can be produced when water is broken down into oxygen and hydrogen: $2 H_2O \longrightarrow 2 H_2 + O_2$, however energy is required to cleave $H - O - H$ bonds. PEC and PC have many advantages as they require no wires or external electronics, they need only low-cost semiconducting absorbers and involve direct energy storage in chemical bonds but it is difficult to find the right materials for efficient PEC and PC processes. Therefore

several studies have been done to find out the most suitable semiconductor materials for photoelectrochemical cells that can utilize solar light effectively. Usually Metal oxides semiconductors (MOS) are used as photoanodes, due to their stability and relatively low cost but their properties (like charge mobility) need to be enhanced. Heterojunctions based on $WO_3/BiVO_4$ semiconductors currently represent the most promising photoanodes for oxygen evolution reaction. WO_3 is an MOS and provides excellent electron mobility but its wide bandgap (2.7 eV) limits its light harvesting efficiency. Whereas $BiVO_4$ is a ternary metal oxide with a narrow bandgap (2.4 eV) but has poor charge separation and surface kinetics. Thus in a $WO_3/BiVO_4$ heterojunction, WO_3 controls the transport properties and $BiVO_4$ the photon collection in the visible region. Moreover the charge transfer properties of oxygen evolution reaction (OER) of $BiVO_4$ can be further improved by depositing OER catalyst. The most promising metals-based catalysts are the Prussian blue (PB)-type materials. They are easily produced, stable within a very large pH range, show a increase in photocurrent, lower photoanodic onset potentials and excellent stability when coupled with $BiVO_4$. In this context, it is important to study the charge transport properties. For this purpose, X-ray absorption spectroscopy (XAS) is the perfect tool as it is able to determine the local atomic and electronic structure of ultra thin layers such as those formed by the mentioned catalysts. Moreover, XAS measurements can be performed under *operando* conditions, as applied potential and illumination. Therefore, in this thesis I will study through *ex-situ* and *in-situ* XAS the atomic and electronic configuration of the $WO_3/BiVO_4/CoFe-PB$ and $WO_3/BiVO_4/CoFeOx$ before, during and after being in a PEC cell in working conditions.

Chapter 2

X-ray Absorption Spectroscopy

X-rays were discovered by Wilhelm Conrad Röntgen in 1895. They are both an electromagnetic wave, with wavelength, λ , in the region of an Ångström ($0.1 \text{ \AA} < \lambda < 10 \text{ \AA}$) and a mass-less non-charged particle, whose energy is in the range of $(1 - 100) \text{ KeV}$. Due to this dual nature, they can interact by three different mechanisms with the electrons in matter showed in Fig. 2.1 : inelastic (Compton) scattering, elastic (Rayleigh) scattering and photo-electric effect. The first two effects are a consequence of the wave nature of light. In fact, X-rays are characterized by the wavelength, close to the atomic dimension, which is 1 – 4 times the radius of the first orbit of the Bohr atom a_0 :

$$a_0 = \frac{\epsilon_0 h^2}{\pi m e^2} \simeq 0.53 \text{ \AA},$$

where ϵ_0 is the vacuum dielectric constant, h is the Plank constant and m is the electron mass, but also to the distances between atoms in condensed matter ($1.5 - 3$) Å and the lattice parameters in crystalline solids ($5 - 10$) Å. As a consequence they can be useful to determine the atomic structure through scattering and interference experiments. On the other hand, photoelectric absorption can be understood on the basis of a particle point of view: matter absorbs a photon and emits an electron. In fact, the range of photon energy for X-rays ($E = hc/\lambda$) is $10^3 \text{ eV} < E < 10^5 \text{ eV}$ and corresponds to the binding one of most elements' core electrons. The binding energy (E_b) in atoms, molecules and solids is

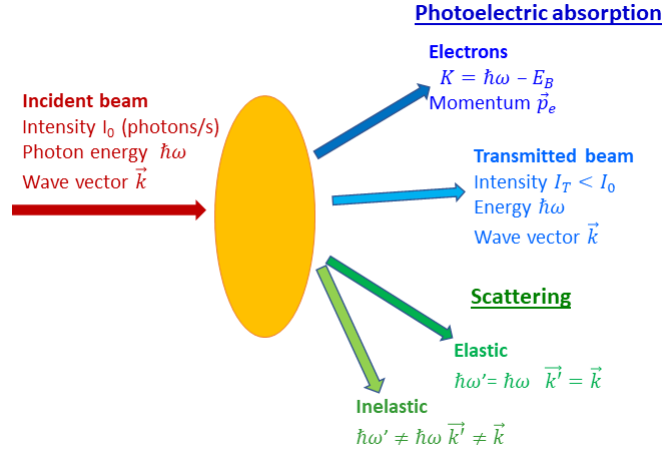


Figure 2.1: Different types of interaction between X-rays and matter.

the energy required to ionize them. For valence electrons, the ones external and involved in the formation chemical bonds, $E_b \approx (1 - 20)$ eV so Ultraviolet photons are sufficient to excite them. Whereas for core electrons, the inner ones and almost not involved by the atomic environment, the E_b are bigger than $(20 - 30)$ eV so X-ray must be used. This technique is called X-ray absorption spectroscopy (XAS). A photon is absorbed by the atom and excites an electron from the core to an empty state above the Fermi level. The absorption cross-section depends on the energy and on the measured element since the photon needs to have the same or higher energy than the core electron to excite it. This gives rise to absorption edges when the photon energy matches the one of the core level, which is unique for each element, making XAS an element-sensitive technique. It can provide information on the local atomic structure, oxidation state and on the electronic structure.

2.1 X-Ray Absorption Spectroscopy

Let us consider a collimated X-ray beam, the number of photons per unit time and unit cross-section is called flux ϕ_0 . If the beam pass through a sample of thickness x , its flux is reduced according to:

$$\phi = \phi_0 e^{-\mu(\omega)x}, \quad (2.1)$$

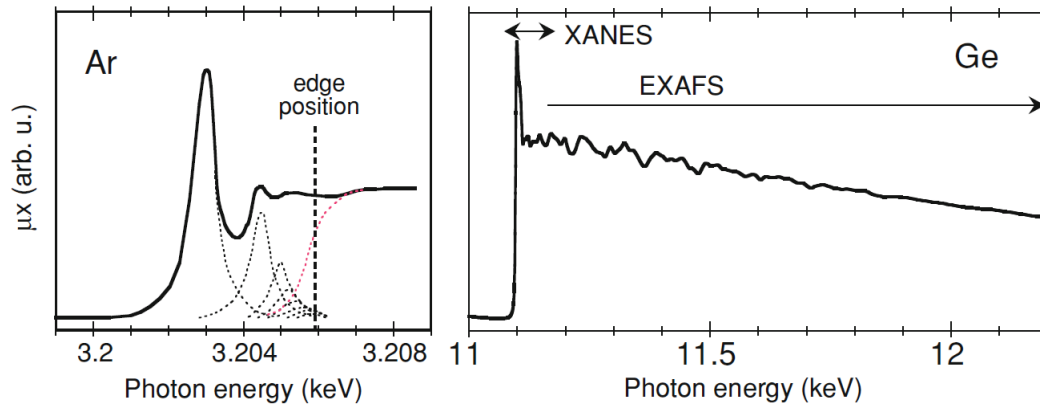


Figure 2.2: Spectra of an isolated atom, K-edge of Argon (left), and the fine structure of Germanium(right). [2]

where $\mu(\omega)$ is the linear attenuation coefficient and depends on the sample composition, density and on the energy of the photons. The main reason for the attenuation of the beam is the absorption of the photons from atoms, which as a result gets ionized or excited. Hence, when the energy of the X-ray photons increases, $\mu(\omega)$ decreases. However, this behavior is disrupted by sharp discontinuities, called absorption edges. They originate when the energy of the photons matches the energy of core electrons, which is also the energy needed to extract an electron from the deeper level. The highest-energy absorption edge is called K edges and correspond to the extraction of an electron from the deepest level (1s level). Since the binding energy of electrons increases monotonically with the atomic number, the energy of edge corresponds to a precise atomic species. After the absorption of X-ray photon, an atom can get excited (if the photons' energy coincide with the difference between an electronic core and an unoccupied bound level) or ionized (if the photon energy is higher than the binding one, so that a photo-electron is ejected from the atom). Near the edge, the $\mu(\omega)$ shows the X-ray Absorption Fine Structure (XAFS). As we can see in figure 2.2 for isolated atoms the photons excite only core electrons to unoccupied levels as a consequence the XAFS is a few eV around the edge. Whereas in molecules and condensed matter the XAFS, strongly influenced by the atoms surrounding of the absorber one, can be even beyond one thousand eV above the edge. We can distinguish different regions in an X-ray absorption spectrum:

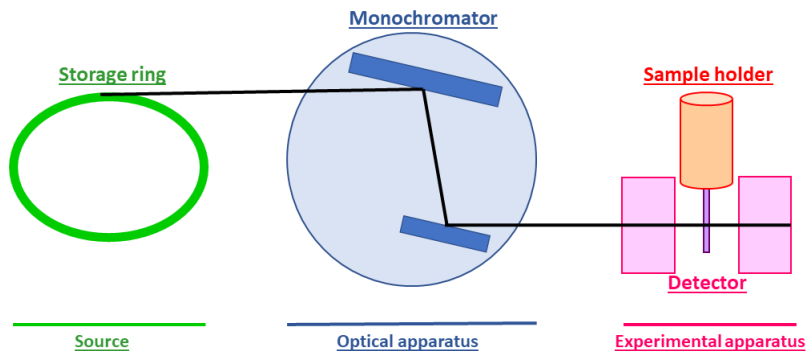


Figure 2.3: Experimental set of a XAS experiment. The X-ray beam passes through a monochromator and a slit to select the wavelength. Then the X-ray is detected before and after traversing the sample.

- The pre-edge and edge region, which is around a few eV around the edge.
- The zone within $(30 - 50) eV$ above the edge is called X-Ray Absorption Near Edge Structure (XANES) which gives information about the local electronic and geometric structure.
- Finally, the region from the XANES up to a thousand eV is said Extended X-Ray Absorption Fine Structure (EXAFS) and contains informations about the local geometric surrounding a specific atomic species.

2.2 Experimental methods

As already mentioned, the feature of interest in XAFS spectra consists in the (small) variation in the absorption coefficient as a function of energy. First of all the source of X-ray must be of the order 10^{10} photons/sec or better within the required energy bandwidth of an eV . Therefore it is usually use a synchrotron radiation source for XAS experiments. As we can see from Fig. 2.3, the X-ray beam after being emitted goes through a monochromator to select the energy of interest. Then it is detected right before and after impinging on the sample. It can be determined directly or indirectly. The direct mode, also said transmission mode, is the most straightforward and it involves a detector (usually a ionization chamber) that measures the X-ray flux before and after

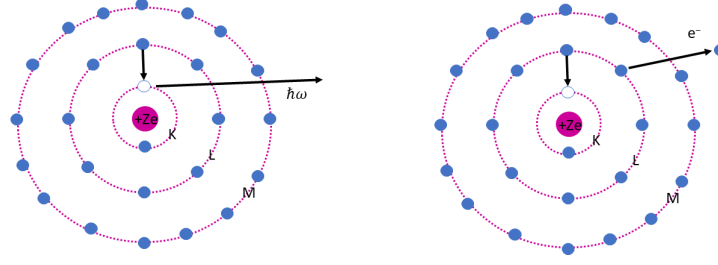


Figure 2.4: Possible outcomes after a photon absorption. On the left it is shown the emission of a characteristic X-ray, whereas on the right there is the emission of an electron called Auger electron. This two outcomes are in competition and can not happen together.

passing through the sample. The transmitted flux, under this condition, is related to the incident one by equation (2.1). In the indirect mode is measured the atomic de-excitation after the photon absorption. In fact as shown in Fig. 2.4 there are two possible outcomes: Emission of a characteristic X-ray with energy

$$E_f = \hbar\omega = E_L - E_K, \quad (2.2)$$

where E_L and E_K are the energy of level L and K. Or ejection of an electron from the surface of the sample with an energy K_A defined as

$$K_A = 2E_L - E_K. \quad (2.3)$$

Due to the short path length (approx. 1000 \AA), this last technique is surface-sensitive, the electrons can be collected in ultra-high vacuum by electrodes or by conversion electron detectors, where the emitted electrons collide with helium gas and produce secondary electrons that can be collected as in ionization chamber.

2.3 Theoretical background

In the photo-electric absorption an atom is initially in its ground state $|\Phi_i\rangle$ of energy E_i . After interacting with the electromagnetic field and absorbing X-rays' energy $\hbar\omega$, the atom uses this energy to excite an electron from the core to an unoccupied outer level or

to the continuum of free state and the atom's final state is $|\Phi_f\rangle$ of energy $E_f = E_i + \hbar\omega$.

The absorption coefficient $\mu(\omega)$ can be expressed as:

$$\mu(\omega) = n\sigma_a = \frac{2\hbar}{\epsilon_0\omega A_0^2 c} n \sum_f \omega_{fi}, \quad (2.4)$$

where n is the number of atoms per unit volume, σ_a is the atomic absorption cross section, $\epsilon_0\omega A_0^2 c/2\hbar$ is the photon flux and ω_{fi} is the probability of transition per unit time from the initial to the final state. Before calculating ω_{fi} , some approximation are needed. In this process the main focus is the elastic transition, in which only the core electron changes its state and the remaining $(N - 1)$ electrons, passive electrons, relax around the core hole. As a consequence the one electron approximation can be used so that $\mu(\omega) = \mu_{el}(\omega)$ and

$$\mu_{el}(\omega) \propto |\langle \Psi_f^{N-1} \psi_f | e^{ik \cdot r} \hat{\eta} \cdot p | \Psi_i^{N-1} \psi_i \rangle|^2 \rho(\epsilon_f), \quad (2.5)$$

where Ψ_f^{N-1} is the Slater determinant of the wavefunctions of the passive electrons whereas ψ, r, p and ϵ_f are wavefunction, vector position, momentum and final energy, respectively. The interaction Hamiltonian is now operating only on one electron. Moreover since the radiation λ is much larger than the size of the system the electric dipole approximation can be used and (2.5) becomes

$$\mu_{el}(\omega) \propto \omega^2 |\langle \Psi_f^{N-1} \psi_f | \hat{\eta} \cdot r | \psi_i \Psi_i^{N-1} \rangle|^2 \rho(\epsilon_f) \quad (2.6)$$

Finally the photo-electron energy is high enough that its interaction with others electrons of the absorbing atoms can be neglected. Hence atomic wavefunction can be factorized in the contributions Ψ_i and Ψ_f of the absorbing electron and Ψ_i^{N-1} and Ψ_f^{N-1} of the passive electrons. Obtaining

$$\mu_{el}(\omega) = n\sigma_{el} = n \frac{\pi e^2 \omega}{\epsilon_0 c} |\langle \psi_f | \hat{\eta} \cdot r | \psi_i \rangle|^2 S_0^2 \rho(\epsilon_f), \quad (2.7)$$

where S_0 is the superposition integral of the passive electrons wavefunctions.

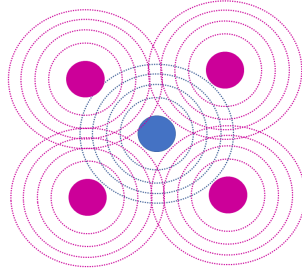


Figure 2.5: Interaction between atoms that originates the fine structure. When an X-ray photon of high enough energy is absorbed by an atom A, a core electron is ejected from the atom. If the absorber atom A is not isolated, the photo-electron can be scattered by a neighbouring atom B. The total photo-electron wavefunction is now a superposition of the outgoing and the scattered waves.

2.4 Extended X-ray Absorption Fine Structure: EXAFS

According to the equation (2.7), μ_{el} reflects the variation of the final photo-electron stationary state $|\Psi_f\rangle$. It contains structural information, evaluated at the core site of the initial state as a function of the photon energy. The most effective approach for XAFS is based on the multiple scattering formalism that allows to use the same interpretation on the entire energy range (from the edge to the EXAFS). However in the EXAFS region, we can simplify further by using the single scattering approximation. If the absorber atom is isolated, the final state $|\Psi_f^0\rangle$ is an outgoing wave whose corresponding absorption coefficient is:

$$\mu_0(\omega) \propto |\langle \psi_f^0 | \hat{\eta} \cdot r | \psi_i \rangle|^2. \quad (2.8)$$

However if the absorber is not isolated, as showed in Fig. 2.5, the photo-electron can interact with the surrounding atoms and undergo scattering. In this region the energy of the photo-electron is much larger than the one of the interaction electron-atom. So we can consider the interactions as weak perturbation to the final state $\psi_f^0 + \delta\psi_f^0$ and (2.8) becomes:

$$\mu(\omega) \propto |\langle \psi_f^0 + \delta\psi_f^0 | \hat{\eta} \cdot r | \psi_i \rangle|^2. \quad (2.9)$$

The normalized EXAFS function is defined as $\chi(k)$

$$\chi(k) = (\mu - \mu_0)/\mu_0. \quad (2.10)$$

By considering the atoms fixed, no thermal motion and atom scattering only once (single scattering approximation), equation (2.10) becomes

$$\chi(k) = \frac{1}{kr_j^2} |f(k, \pi)| \text{Sin}[2kr_j + \varphi + 2\delta_1]. \quad (2.11)$$

The absorption coefficient has a sinusoidal modulation as a function of k and the period of oscillation depend on r_j . If the backscattering atoms can be grouped into coordination shells, where each contains N_j atoms of the same species at same distance R_j from the absorber, equation (2.11) becomes:

$$\chi(k) = \sum_{j=\text{shells}} N_j f_j(k, r_j, \pi) \sin 2kr_j + \varphi_j + 2\delta_1, \quad (2.12)$$

where we separate and sum the contribution of each coordination cell. The X-ray absorption process takes place in a time scale smaller than the period of thermal vibrations so XAS measures. By considering small displacement and not too high temperatures, the distribution of distances follows a gaussian distribution and it has an effect on the EXAFS function of:

$$\chi(k) \propto \sin 2kr_j e^{-2k^2\sigma^2}. \quad (2.13)$$

As a consequence the thermal motion's effect is to introduce a term $e^{-2k^2\sigma^2}$ that attenuate the EXAFS oscillations, with

$$\sigma^2 = \langle [\hat{R}_j \cdot (\vec{u}_j - \vec{u})_0]^2 \rangle \quad (2.14)$$

called EXAFS Debye Waller factor, which is sensitive only to uncorrelated atomic motion and it's different from the Debye Waller factor used in crystal diffraction of X-ray.

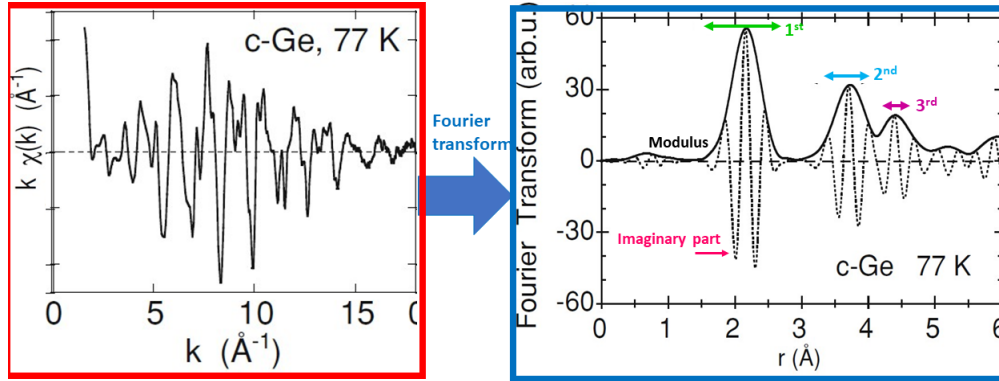


Figure 2.6: Effect of Fourier transformation on EXAFS signal. On the left is displayed the EXAFS signal whereas on the right the Fourier transformation of the crystalline germanium at 77K [2].

Relaxation of orbitals and excitation of electron destroy interference and reduce the EXAFS effect. It is necessary to multiply the $\chi(k)$ by

$$S_0^2 = |\langle \Psi_i^{N-1} | \Psi_f^{N-1} \rangle|^2, \quad (2.15)$$

which is usually in the range between (0.7 – 0.9). Furthermore the core hole has a lifetime τ after which it decays and emits fluorescence photons or Auger electrons and the photoelectron wave function will change due to the central atom potential. In order to take into account the effect of the core lifetime and the inelastic scattering, the EXAFS function will be multiplied by:

$$\exp^{-2r_j/\lambda}, \quad (2.16)$$

in which $\frac{1}{\lambda} = \frac{1}{\lambda_h} + \frac{1}{\lambda_e}$. As a conclusion for a powder or amorphous sample, the "standard" EXAFS formula is:

$$\chi(k) = S_0^2 \sum_{j=shells} N_j f_j(k, \pi) \sin[2kr_j + \Phi_j + 2\delta_1] e^{-2k^2\sigma_j^2} e^{-2r_j/\lambda}, \quad (2.17)$$

where as already said N_j is the coordination number, r_j is the interatomic distance ($\sim 0.01 \text{ \AA}$) and σ_j^2 is the Debye Waller factor. By applying this last formula it is possible to determine experimentally these local structural parameters. To analyse the entire EXAFS

signal $\chi(k)$ the Fourier transform and back-transform of the signal are used. The Fourier transform from the space of wavevectors k to the conjugate space of distances r is shown in Fig. 2.6 and performed through the integral:

$$F(r) = \int_{k_{min}}^{k_{max}} \chi(k)W(k)k^n e^{2ikr} dk, \quad (2.18)$$

where $W(k)$ is a window function that reduces the spurious oscillations, the factor k^n is used to balance the low-k and high-k regions of the spectrum. The limits k_{min} and k_{max} are chosen to exclude both the low-k signal. The Fourier transform $F(r)$ of (2.18) is a complex function composed of a real and an imaginary part whose modulus is characterized by peaks in correspondence of the leading frequencies $2r$ of the $\chi(k)$ signal, in general the highest peaks correspond to single scattering paths (coordination shells). However, it is not a true radial distribution function because the positions of the peaks are at slightly shorter distances than the real distances, due to the phase-shifts.

2.5 X-ray Absorption Near Edge Structure (XANES)

XANES is a unique local probe, in fact its spectral features are stronger near the edge, making the XANES signal less sensitive to data statistic and on the samples quality. This makes XANES suitable for studies on low quality or diluted samples, like, for example, natural ones; XANES is also sensitive to weak changes of valence state, coordination chemistry, local structure and ligand symmetry around the photoabsorber, so it can be used as fingerprints to identify precisely chemical species in mixtures and complex materials. Finally, sometimes it is also possible to probe bindings of light elements hardly visible by XRD due to the rapid decrease of the backscattering amplitude functions. Despite all this advantages, to study the absorption edge it is needed more in-depth theory as the progressively longer mean free path of low energy photoelectrons enhances the multiple scattering terms and the finest details characterizing the DoS, density of states, close to the Fermi level and the interatomic potentials become definitively relevant. To explain

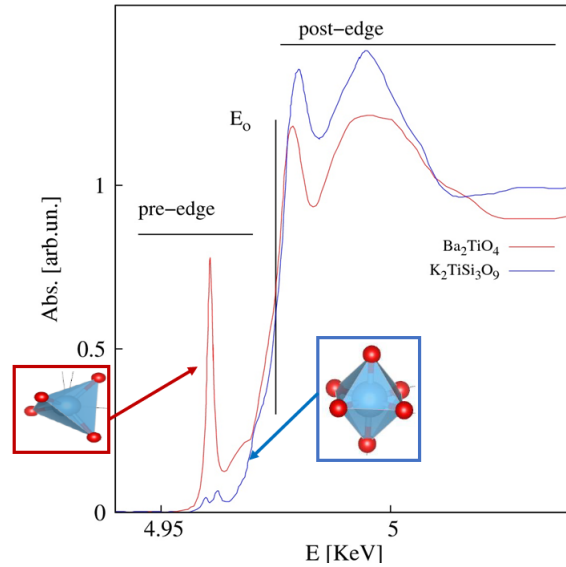


Figure 2.7: Different Ti K-edge XANES produced by different Ti^{4+} coordination geometries [2].

better the information which can be obtained from XANES it is common to divide the spectrum in three main regions:

- Pre-edge ($E < E_0$), the region before the edge, whose features mostly originates from dipole allowed transition to bound localized state. In this region the hybridization of the electronic levels is strongly affected by details of the crystalline field caused by the ligand geometry. This gives rise to large differences also for elements in the same valence state but having different local structure.
- Edge ($E = E_0$), the position of the absorption edge is related to the oxidation state of the photoabsorber, higher oxidation state raises E_0 . It is possible to recognize the valence state of the photoabsorber by looking at the edge position (as shown in Fig. 2.8). Moreover the edge's shape is often characteristic of the chemical environment and ligand geometry, then it can be used as a fingerprint of a particular chemical specie.
- Post-edge ($E > E_0$) region corresponds to photoelectrons excited in the continuum states and it provides valuable details about local structure and coordination geom-

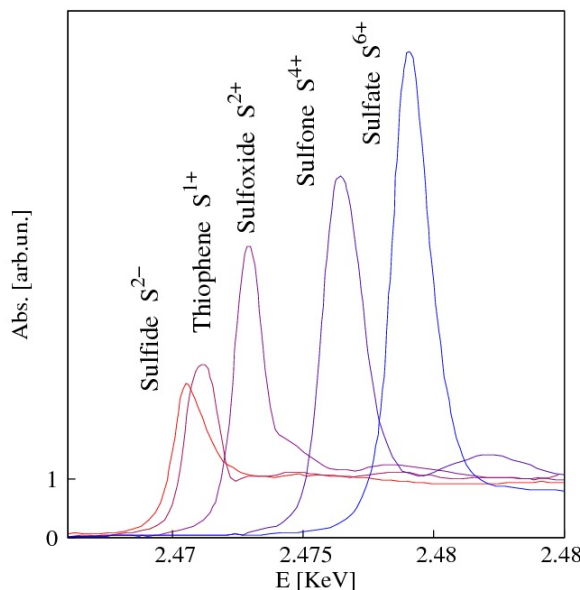


Figure 2.8: Different compounds of Sulfur produce different Sulfur K-edge XANES spectra and shifted edges [2].

etry.

XANES calculations can be extremely time consuming in case of complex structures. However a phenomenological interpretation of XANES features very intuitive and immediate: First of all it's necessary to check the edge position since it may be shifted as a function of their oxidation state. Therefore, After an energy calibration on reference compounds, the edge position can be used to rapidly assign the oxidation state of the absorber. Then to quantify the relative amount of chemical species in mixtures and multi-phase compounds it can be used the LCA (Linear combination analysis). It exploits the fact that the shape of the XANES reflects the chemical environment of the absorber, then it can be compared with the spectra of reference compounds. This is a simple method but it requires a proper set of good quality spectra measured, preferably during the same experimental run, on reference compound. Then there are many features around the edge that can be interpreted. For example shape, intensity and position of the XANES peaks as a function of environmental parameters may provide structural and electronic details, specially in comparison with reference systems. Another feature of XANES is linear dichroism, which

is the dependence of a physical quantity on the orientation of sample and direction of linear polarization of the probe beam. It can provide information on the orientation of molecular orbitals with respect to probe beam. In a simple case, the intensity is maximum when the orbital is oriented in the direction of polarization.

2.6 Fluorescence Spectroscopy

Fluorescence spectroscopy is a method to determine a chemical species or its concentration in solution, based on its fluorescent properties. In this technique, a beam passes through a solution, exciting an electron from the core to an empty state above the Fermi level, the atom will have a core hole and as a consequence will be unstable. Spontaneously it will relax, filling the core hole with an electron from an upper level and thereby reducing its energy. As already said and showed in Fig. 2.4 there are two de-excitation mechanisms possible. The relaxation energy can be released as an outgoing X-ray photon (fluorescence mechanism) with energy expressed by equation (2.2) or can be used to eject an (Auger) electron from an upper level (Auger mechanism) with kinetic energy (2.3). The intensity of the fluorescence is proportional to the impinging flux, to the solid angle of detector acceptance and most important to the absorption coefficient. The energies of fluorescence photons depend on the energies of the electron levels and unequivocally identify the atomic species. As a consequence measuring the fluorescence emitted by the sample it is possible to get information about the type and concentration of multiple chemical species simultaneously.

Chapter 3

Photoelectrocatalysis

Nowadays the need for renewable energy sources has become imperative. Generally, renewable energy sources include wind, hydropower, bioenergy, geothermal, and solar energy. However, it is very challenging to reduce the cost of solar energy conversion processes and devices to contribute significantly and to store solar fuel efficiently. One of the most attractive possibilities is to store the solar energy in the form of a chemical fuel. The energy of a visible light photon is $(1 - 3) eV$, which is more than enough for most chemical reaction to happen. Examples of chemical fuels include hydrogen, methane, methanol, gasoline, diesel, etc. However, except for hydrogen, all of these examples require a source of carbon. The ideal solution would be to capture the CO_2 in the atmosphere and to reuse it by synthesizing fuels with sunlight as energy source. However direct photo(electro)chemical conversion of CO_2 to a fuel seems to be even more challenging, as the electrochemical half-reactions for the conversion of CO_2 to, e.g., methanol or methane involve complex six- and eight-electron transfer steps, respectively. As a consequence the conversion and storage of solar energy into molecular hydrogen appears to be a much more attractive choice. The splitting of water into hydrogen and oxygen is an uphill reaction, producing a renewable and environmentally friendly fuel whose major combustion outcome is plain water, with zero associated emission. Moreover, hydrogen gas has the highest mass-to-specific energy ratio among the other fuels. Since different methods have been

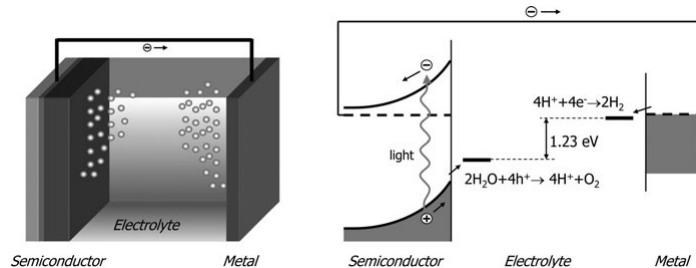


Figure 3.1: Illustration of a photoelectrochemical cell that consists of a semiconducting photoanode and a metal cathode. The corresponding energy diagram is shown in the right [3].

used to produce hydrogen fuel from water splitting, in this thesis I will focus on one of the most promising, the photoelectrocatalytic water splitting. i.e the electrolysis of water promoted by one or more semiconductor photoelectrodes, able to harvest the incoming photons and direct the photogenerated charges towards the splitting of H_2O into H_2 . This technique needs water, low-cost semiconducting absorbers and involve direct energy storage in chemical bonds. Furthermore hydrogen and oxygen are produced at separate electrodes and this allows easy separation of these gases in contrast to the more common photocatalytic approach, where no physical separation is achieved due to the homogeneous environment.

3.1 Principle of Photoelectrocatalysis

Fig. 3.1 shows a simplified energy diagram of a photoelectrochemical (PEC) cell based on a single semiconducting photoanode and a metal cathode submerged in a electrolyte. The main component of the PEC cell is the semiconductor, which converts incident photons to electron-hole pairs. After illuminating it, electrons and holes are generated on the photoanode. The photogenerated pairs, due to the presence of an electric field inside the semiconductor, are separated. The photogenerated electrons are swept toward the conducting backcontact and are transported to the metal counter-electrode via an external wire. The photogenerated holes are pushed toward the semiconductor/electrolyte interface, where they oxidize water to form oxygen gas. So two half-reactions are involved and

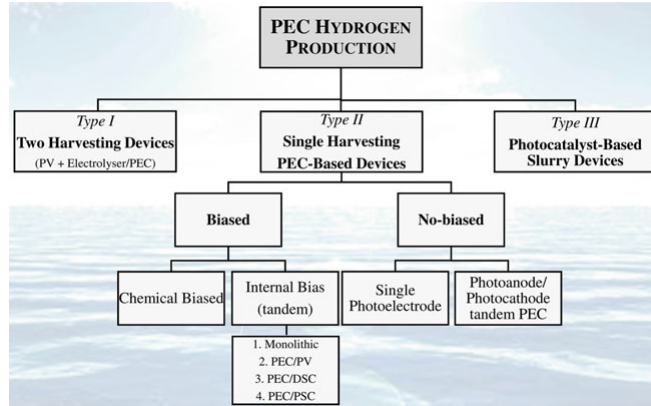
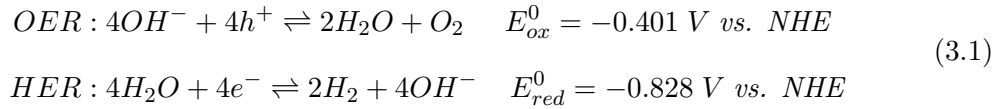
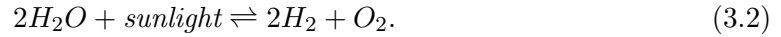


Figure 3.2: Photoelectrochemical device configurations for solar hydrogen production [12].

they must happen simultaneously: the oxygen evolution reaction (OER) and the hydrogen evolution reaction (HER). Considering the case of an alkaline electrolyte, reduction and oxidation reactions can be written as



and the overall water splitting reaction is



Since this reaction has a positive Gibbs free energy, it is a non-spontaneous reaction. Therefore, the water-splitting reaction needs to apply a potential of at least $(1.23)\text{V}$ versus reversible hydrogen electrode (RHE) for it to happen.

Fig. 3.2 summarizes the configurations of PEC devices for solar hydrogen production:

- Type I: It combines two physically separated devices to directly drive electrolysis; the only coupling between the PV and electrolysis components is electrical. This configuration prevents the degradation of PV by the water. It has not a stability issues (PV contact with electrolyte solution is avoided) however it is more complex and expensive to build for large-scale deployment

- Type II: They are divided into biased and non-biased systems. In the biased ones, cells operate under illumination in combination with an appropriate bias source to directly promote hydrogen generation; The bias can be both chemical or internal. Whereas non-biased devices are based on single photoelectrodes or two photoelectrodes (photoanode and photocathode) in a tandem arrangement. They are cheaper to build, can be used cheap non transparent substrate, however they have poor utilization of the solar spectrum since is needed a large bandgap ($E_g > 1.7eV$).
- Type III: It consists of photoactive semiconductor particles (photocatalysts) free-floating as slurry in a solution bed. It has more efficient utilization of the solar spectrum but it is way more complex than the other two (need a transparent conducting substrate, need adequate transmittance from front electrode, photocurrent limited by the component generating the smallest current value ecc.)

Another widely applied method is intensity modulated photocurrent spectroscopy (IMPS), which involves modulation of the intensity of illumination incident on a photoelectrode and measurement of the magnitude and phase shift of the resulting photocurrent relative to the periodic illumination. The basic idea of IMPS is to analyze, as a function of frequency, the amplitude and phase of the photocurrent generated by the system in response to a sinusoidal modulation of the incident light intensity, which perturbs the surface concentration of the photogenerated carriers. The result of IMPS measurements is the frequency dependent photocurrent admittance, $Y_{pc}(w)$, which is the relation between the excitation by a dynamic variation of the light intensity and the response of the photocurrent density. It can be both positive or negative which means that can be assigned to charge transfer and recombination, respectively, thereby providing a measure for the charge transfer (or injection) or transmission efficiency. The normalized $Y_{pc}(w)$ is a quantity that describes the number of charge carriers divided by the number of incident photons and contains information on the efficiency of the photoelectrode.

Finally Fig. 3.3 displays the typical configuration for the evaluation of the photoanode activity under simulated sunlight. The voltammogram at the bottom displays the main

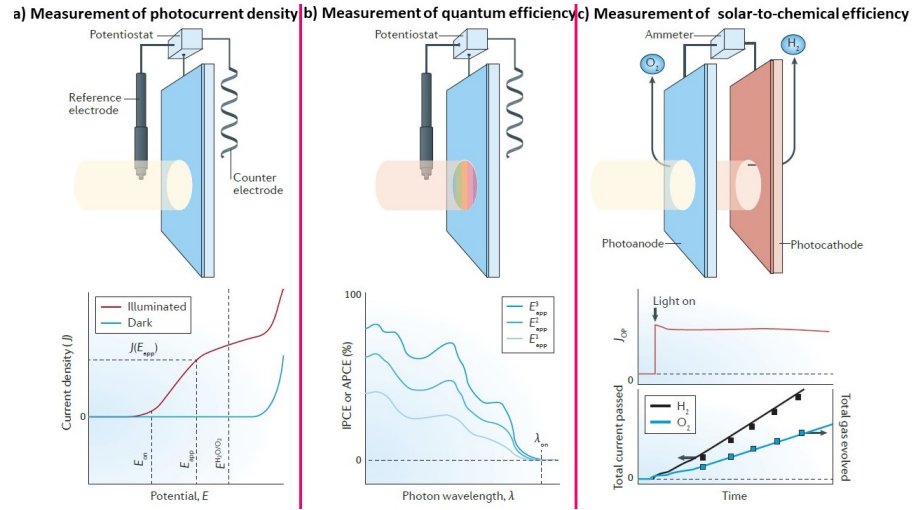


Figure 3.3: Different configuration of PEC cells for the evaluation of the photoanode activity under simulated sunlight [10].

figures of merit, such as the photocurrent J and the onset potential E_{on} . The most common method is the one used to measure the photocurrent density J_{ph} displayed in part a). The photocurrent is produced by the photoelectrode in an electrolyte as a function of the applied potential, E , using a potentiostat. The potential E is reported relative to a reference electrode, and the current flows between the photoelectrode and the counter-electrode during testing. The onset potential, E_{on} , for the photocurrent can be defined from the plot. Whereas panel b) shows the quantum-efficiency metrics, where are measured quantity like the incident (or absorbed) photon-to-current efficiency, IPCE (or APCE). This technique is useful for determining which photon energies contribute to the solar photocurrent. The wavelength, λ , of the monochromatic incident illumination is varied whereas the applied potential is fixed. Then the photocurrent density J_{ph} is measured at each wavelength. Lastly to measure the solar-to-chemical conversion efficiency it is needed a two-electrode configuration, as shown in section c) of Fig. 3.3. Measuring the operating photocurrent density, with an ammeter as a function of time gives an indication of the stability of the device. The integrated J_{op} gives the total charge passed, which can be compared with the total amount of gas evolved to give the faradaic efficiency, η_F . For the water-splitting reaction, the overall solar-to-hydrogen conversion efficiency (STH) is

calculated as

$$STH = j_{op} \times (1.23 \text{ V}) \times \frac{\eta_F}{P_{in}} \quad (3.3)$$

where 1.23 V corresponds to the Gibbs free energy of the reaction.

3.2 Charge Carriers and Doping

Under equilibrium conditions (no illumination and no net current flow), the concentration of free electrons in the conduction band and free holes in the valence band is given by:

$$n = N_C e^{-(E_C - E_F)/kT} \quad \text{with} \quad N_C = 2 \left(\frac{2\pi m_e^* kT}{h^2} \right)^{3/2}. \quad (3.4)$$

$$p = N_V e^{-(E_F - E_V)/kT} \quad \text{with} \quad N_V = 2 \left(\frac{2\pi m_h^* kT}{h^2} \right)^{3/2}, \quad (3.5)$$

These equations are valid even if the semiconductor is doped but not if it is degenerate. Equations (3.4) and (3.5) originate from the nearly free electron model, are useful for describing the behavior of semiconducting photoelectrodes however they may not be entirely accurate for transition metal oxides. To improve the conductivity the semiconductors are often doped. In metal oxide photoelectrodes, shallow donors and acceptors are almost always necessary because of the low intrinsic charge carrier mobilities. In fact the conductivity of the material is given by $\sigma = ne\mu_e + pe\mu_h$, so increasing n or p will compensate for a small value of μ_e or μ_h . An example of donor-type dopants is Ti^{4+} on a Fe^{3+} site in Fe_2O_3 . If the dopant level is within $\sim 2kT$ of E_C or E_V , it will be almost fully ionized at room temperature. Otherwise for deep donors the degree of ionization can be calculated with:

$$\frac{N_D^*}{N_D} = \frac{1}{1 + g_D e^{(E_F - E_D)/kT}}, \quad (3.6)$$

where E_D and g_D are correspondingly the donor energy and the degeneracy factor that reflect the multiplicity of the energy state. Under the assumption that $n = N_D^+$, the following expressions relate the free electron concentration directly to the position of the

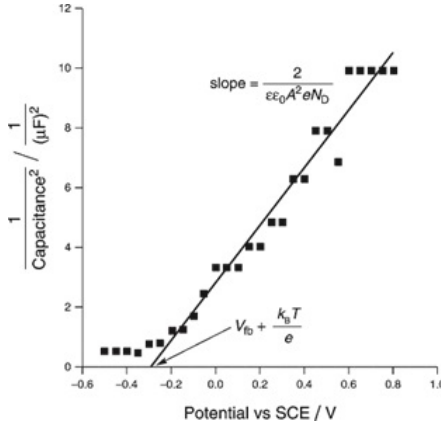


Figure 3.4: Mott-Schottky plot for ZnO in the semiconductor-electrolyte, $7 \cdot 10^{-4} M K_3[Fe(CN)_6]$ [9].

donor level in the bandgap

$$n = \frac{N_{\zeta}}{2} \sqrt{1 + \frac{4N_D}{N_{\zeta}}} - 1 \quad \text{with} \quad N_{\zeta} = \left(\frac{N_C}{g_D} \right) e^{-(E_C - E_D)/kT}. \quad (3.7)$$

It is possible to find analogous equations for acceptors-doped materials.

3.3 Space Charges and Band Bending

One of the key features of a semiconductor is the presence of a built-in electric field. The formation of a space charge is explained by a semiconductor being brought into contact with a metal or another semiconductor. The movement of charges is due to different Fermi levels between the two materials. The charge diffusion will go on until the Fermi level is the same for both the materials. To understand the PEC cell is important to know the potential distribution in the depletion layer and where it came from. The starting point for the derivation is Poisson's equation in one dimension that describes the relationship between charge density and potential difference in a phase. Then using the Boltzmann distribution to describe the distribution of electrons in the space charge region and Gauss' law relating the electric field through the interface to the charge contained within that

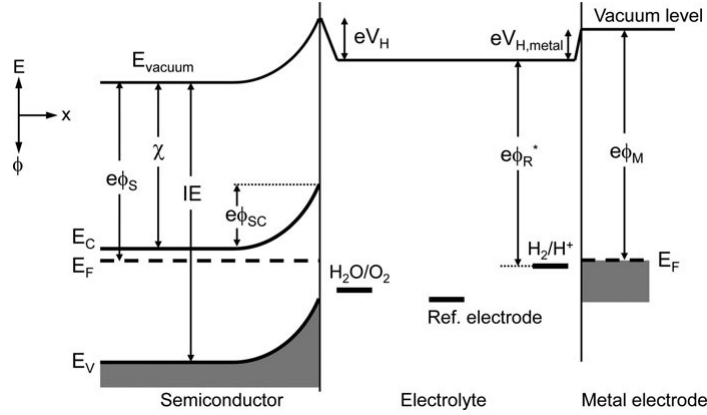


Figure 3.5: Energy diagram for a PEC cell based on a n-type semiconductor and a metal counter electrode. [3].

region, Poisson's equation can be solved to give the *Mott-Schottky* equation:

$$\frac{1}{C_{SC}^2} = \left(\frac{dQ_{SC}}{D\Phi_{SC}} \right)^{-2} = \frac{2}{\epsilon_0 \epsilon_r e N_D A^2} \left(\phi_{SC} - \frac{kT}{e} \right), \quad (3.8)$$

C and A are the interfacial capacitance and area. Therefore, a plot of $1/C_{SC}^2$ as a function of the applied potential should result in a straight line (as in Fig. 3.4) from which can be determined both the donor density of the semiconductor, from the slope, and the flat band potential, from the intercept on the V axis. Typical values for C_{SC} are (10–1000) nF/cm^2 .

3.4 The Band Diagram

An example of a cell composed of a n-type photoanode and a metal counter electrode is shown in Fig. 3.5. The energy reference of an electron is chosen in vacuum at infinite distance. It is important to note that the vacuum level bends in the presence of an electric field which means that it follows the potential gradients that are present in the PEC cell. This is a consequence of the convention that the electrochemical potential (or Fermi energy) of the electrons is constant when the system is in equilibrium. The most important parameters for the semiconductor are the band positions, the amount of band bending and the difference between E_C and E_F . The latter depends on the free electron concentration in the bulk through equation (3.4). The energy diagram shows clearly if a specific reduction

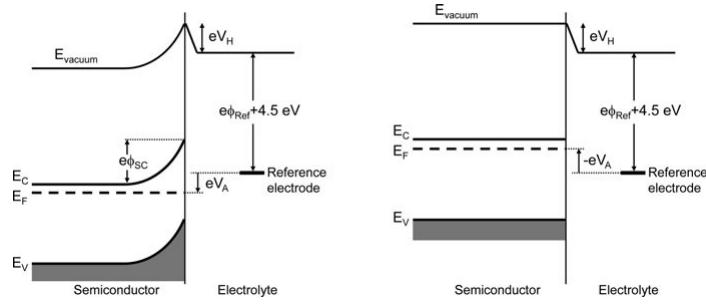


Figure 3.6: Effect of applying a bias voltage V_A to an n-type semiconductor electrode. Any change in applied potential falls across the space charge layer, whereas V_H remains constant. In the picture on the left, a positive potential is applied to the semiconductor. The band bending can be reduced to zero When a sufficiently negative bias is applied [3].

or oxidation reaction at the semiconductor surface is thermodynamically possible. In the example of Fig. 3.5, the photogenerated holes are able to oxidize the water if the redox energy of H_2O/O_2 is above the top of the valence band. Similarly, only electrons with an energy higher than the redox energy can reduce the corresponding species in the electrolyte. In conclusion the reduction or oxidation power of the semiconductor can be determined by measuring the potential (the Fermi level) of it with respect to that of a reference electrode.

3.5 Applying A Bias Potential

When the bias is applied with respect to a reference electrode, the potential difference will be distributed over the space charge layer and the Helmholtz layer. Since these layers act as two capacitances in series the C_{tot} will be:

$$\frac{1}{C_{tot}} = \frac{1}{C_{SC}} + \frac{1}{C_H}. \quad (3.9)$$

Both layers have the same charge Q located at the inner Helmholtz plane, and since $C = Q/V$, the potential distribution is given by

$$\frac{\Delta V_{SC}}{\Delta V_H} = \frac{C_H}{C_S C}. \quad (3.10)$$

Since $C_H \gg C_{SC}$, any change in applied bias will fall across the depletion layer of the semiconductor. Applying a positive bias to an n-type semiconductor the depletion layer will increase. For a p-type semiconductor, a negative bias is required to increase the depletion layer. In Fig. 3.6 is shown that by applying a positive bias to an n-type semiconductor, it results in an increase of the depletion layer. Whereas for a p-type semiconductor, a negative bias is required to increase the depletion layer.

3.6 pH Dependence of The Band Edges

It is important to know that even if V_H is not affected by the applied bias potential, it depends on the pH of the solution. The positions of the band edges shift with -59 mV per pH unit with respect to the redox potentials in the electrolyte. This could seem a useful property, in fact if the reduction of a certain species is not possible because the conduction band is too low in energy, it could be increased by making V_H more negative, increasing the pH toward more alkaline values. However a consequence would be also the increase of E_V , reducing the oxidation power of the semiconductor. The reduction and oxidation potentials depend in the same way on the pH as the band positions. Therefore the band positions of most metal oxides are fixed with respect to the water redox potentials. The knowledge of the band edge positions at the surface is very useful, since they determine the maximum reduction and oxidation potentials of the photogenerated electrons and holes in a semiconductor.

3.7 The Photoelectrochemical Cell Under Operating Conditions

Fig. 3.7 shows the energy diagram of a PEC cell in the dark and under illumination. In this example, the H_2O/O_2 redox couple is assumed to be the most active species and therefore dominates the electrochemical potential of the solution in the dark. Since the semiconductor and metal are electrically connected, the Fermi levels will adjust to a

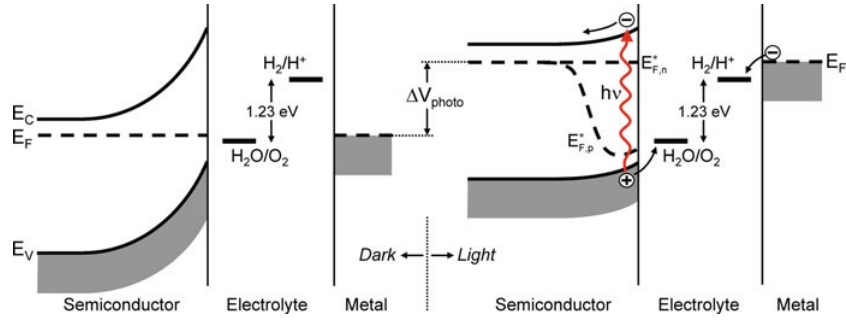


Figure 3.7: Band diagram for a PEC cell based on an n-type semiconducting photoanode that is electrically connected to a metal counter electrode. Illumination raises the Fermi level and decreases the band bending. The Fermi level near the semiconductor/electrolyte interface, splits into quasi-Fermi levels for the electrons and holes [3].

value close to E_{ox} . Upon illumination, electron–hole pairs are created and the Fermi level increases with ΔV_{photo} , the internal photovoltage. Since the system is no longer in equilibrium, the notion of quasi-Fermi levels is needed. Quasi-Fermi levels are a direct measure of the concentration of electrons and holes at a certain point x in the semiconductor, and are defined as:

$$\begin{aligned} n &= n_0 + \Delta n = N_C e^{-(E_C - E_{F,n}^*)/kT}, \\ p &= p_0 + \Delta p = N_V e^{-(E_{F,p}^* - E_V)/kT}, \end{aligned} \quad (3.11)$$

where, n_0 and p_0 are the equilibrium carrier concentrations in the dark, and Δn and Δp are the additional carriers created by illumination. For an n-type semiconductor, $n = n_0 + \Delta n \approx n_0$ and $p = p_0 + \Delta p \approx \Delta p$ so that $E_{F,n}^*$ remains horizontal whereas $E_{F,p}^*$ departs from the bulk Fermi level in the active region. The quasi-Fermi level is often interpreted as a thermodynamic driving force that leads processes. However they only account electrons and holes in the conduction and valence bands, not in the occupation of surface or bulk defect states. This limits their predictive value for reactions in which these states are involved.

3.8 Photocurrent–Voltage Characteristics

One of the most often used models was reported by Gärtner, who derived the following expression for the photocurrent in a semiconductor under reverse bias:

$$j_G = j_0 + e\Phi \left(1 - \frac{\exp(-\alpha W)}{1 + \alpha L_p} \right), \quad (3.12)$$

where Φ is the incident light flux, α is the absorption coefficient (assuming monochromatic illumination), W is the depletion layer width, L_p is the hole diffusion length, and j_0 is the saturation current density. The model assumes that there is no recombination in the SCR and at the interface. To account also the recombination is better to use Reichman model [7]:

$$j_V = \frac{j_G - j_0 \exp\left(\frac{-e\eta}{kT}\right)}{1 + \frac{j_0}{j_v^0} \exp\left(\frac{-e\eta}{kT}\right)}, \quad (3.13)$$

where j_V^0 is the hole transfer rate at the interface and j^0 is the saturation current density (the hole current in the valence band at $x = 0$ when $\Phi = 0$). The quantity η is the overpotential, defined as the difference between the applied potential and the open-circuit potential under illumination. This model includes the possibility of recombination in the SCR, which could become important when the photovoltage becomes large enough for the bands to flatten. It can also be used to model the effect of the slow hole transfer kinetics that are often observed for metal oxides such as hematite. The saturation current density $j_0 = (eL_p N_C N_V / \tau N_D) \exp(-E_g/kT)$ plays an important role in Reichman's model, especially if semiconductors have narrow-bandgap, large hole diffusion lengths and low donor densities. If the bandgap exceeds ~ 1.8 eV, which is the case for almost all metal oxides, j_0 becomes negligible therefore Reichman and Gärtner are indistinguishable.

3.9 Semiconducting Photoelectrode Materials

The key component for PEC systems is the semiconductor photoelectrode and it is difficult to find the right materials for efficient process. The ideal photoelectrode should

fulfills more tasks simultaneously:

- Strong oxidation stability.
- Stable in an aqueous solution.
- Have a potential at low cost.
- High carrier separation and transfer efficiency.

At the moment it does not exist a semiconductor with such properties so usually composite photoelectrodes are used where different materials fulfill different functionalities.

It is really important to look at the electronic band structure as many features can be deduced. The first insight is the nature of the optical transition, which can be both direct or indirect.

Another observation can be obtained from the electronic band structure about the mobility of charge carriers μ , which is related to the width of the conduction and valence bands. In general more overlap between atomic wavefunctions results in broader bands and easier transport of free charge carriers through the material. This can be quantified via the curvature of the individual bands $\frac{\delta^2 E}{\delta k^2}$, which is directly related to the effective mass m^* and mobility of the charge carriers

$$m^* = \frac{\hbar^2}{\frac{\delta^2 E}{\delta k^2}} \quad \text{and} \quad \mu = \frac{q\tau}{m^*}. \quad (3.14)$$

Wide bands that are strongly curved have a high charge carrier mobility. The third insight that can be obtained from the electronic band structure is the density-of-states (DOS), number of allowed electronic states per unit of energy interval. From the DOS representation is possible to identify the various bands and their widths. Moreover the total number of excitations per second is proportional to the DOS at the occupied ground state (the initial state), multiplied by the transition probability to the final state λ_{if} (given by Fermi's rule):

$$\lambda_{if} = \frac{2\pi}{\hbar} |M_{if}|^2 g_f. \quad (3.15)$$

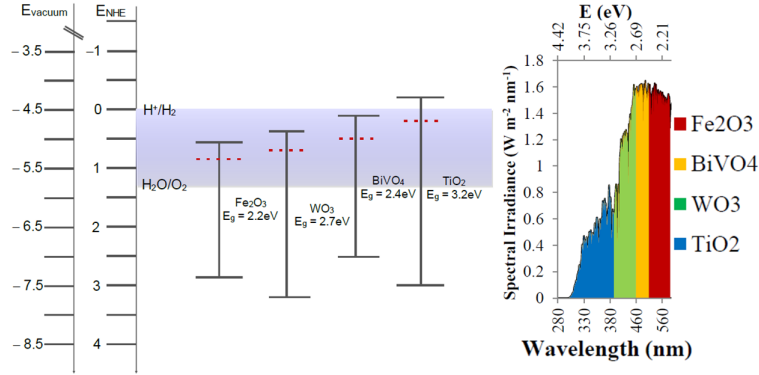


Figure 3.8: On the left: Band positions for n-photoanode materials. On the right: Solar absorption of n-photoanodes materials [8].

Therefore DOS also gives an idea of the optical transition probabilities between various bands. As photoanodes are mainly used n-type metal oxides like TiO_2 , WO_3 , $BiVO_4$, and Fe_2O_3 . They have a band gap range (2.1 – 3.2) eV therefore they absorb largely the UV and the visible region of the solar spectrum (as shown in 3.8). Fig. 3.8 displays a diagram suggesting the theoretical band positions from several literature sources relative to the NHE (pH 0) of n-type metal oxides (with Fermi levels arbitrarily placed).

3.9.1 Photoanode: Bismuth vanadate on tungsten trioxide

In recent years, as a n-type semiconductor material, $BiVO_4$ has been widely studied in the field of PEC technology because of various advantages, such as good light absorption performance, higher stability, suitable positions of the conduction and valence band (showed in Fig. 3.10) and low cost. Even if $BiVO_4$ exhibits visible light absorption capability and a high photocurrent of up to 4.5 mA cm^{-2} , it has poor charge transfer and fast recombination issues. Therefore it is often coupled with other semiconductor; $WO_3/BiVO_4$ is currently the most successful hetero junction with an external quantum efficiency (EQE) of over 90%. In fact $BiVO_4$ absorbs visible light whereas WO_3 acts as electron transfer agent. Tungsten trioxide (WO_3) is a metal-oxide-semiconductor with excellent electron mobility and good chemical stability in acidic aqueous solutions; how-

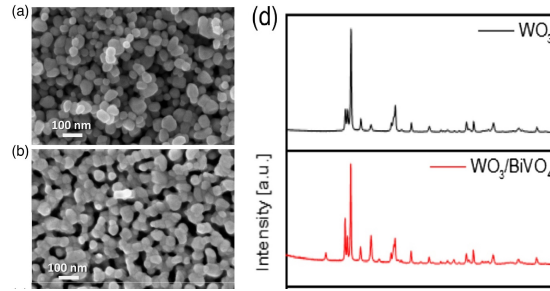


Figure 3.9: FESEM micrographs of a) WO_3 , b) $WO_3/BiVO_4$. d) XRD pattern of the prepared photoanodes and reference patterns for WO_3 and $BiVO_4$ [23].

ever it has a bandgap ($\sim 2.7eV$) which limits its efficiency (LHE) to about 12% of the solar spectrum. One of the possible structure is the colloidal WO_3 (Fig. 3.9 a), characterized by a nanostructured morphology made of aggregated nanoparticles synthesized together in a porous 3D network. Moreover from the X-Ray diffraction in Fig. 3.9 d) films of WO_3 exhibit a monoclinic structure while $BiVO_4$ films show the typical monoclinic clinobisvanite structure. As already said, when a large band gap semiconductor is coupled with another one with a small band gap having a more negative conduction band (CB) level, the CB electrons goes from the small band gap semiconductor into the large one enhancing the lifetime of the photoinduced hole by spatially separating them from the electrons transferred to the electron collector WO_3 . Since $BiVO_4$ has a narrow band gap ($2.4 eV$) and its conduction band is more negative than that of WO_3 , the coupling $WO_3/BiVO_4$ photoanodes could be suitable for efficient photoelectrochemical cell application under visible irradiation. Moreover, the fast charge transport in WO_3 facilitates

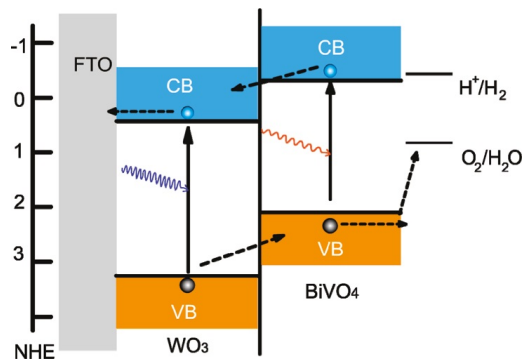


Figure 3.10: Energy diagram of the $WO_3/BiVO_4$ heterojunction (at pH 7) and electron transport process [6].

electron extraction from $BiVO_4$ resulting in photocurrent improvement. In Fig. 3.11 there is a set of linear-sweep voltammograms (with respect to normal hydrogen electrode NHE scale) recorded on planar thin films illuminated through the substrate (back-side illumination) with chopped light. Upon illumination, a single $BiVO_4$ layer (green line - c) showed a photocurrent in the range of $20\mu A/cm^2$, while a $\sim 700nm$ thick WO_3 layer (blue line, b) showed pronounced photocurrent starting at $0.1 V$ which continued to increase to $0.4 mA/cm^2$ at $+1.0 V$. With the $BiVO_4$ layer placed upon the WO_3 layer, individual layer thicknesses unchanged, the $WO_3/BiVO_4$ heterojunction films (red line, a) showed a significant photoresponse enhancement which started at $-0.4 V$ and reached a photocurrent density of $0.8 mA/cm^2$ at $+1.0V$.

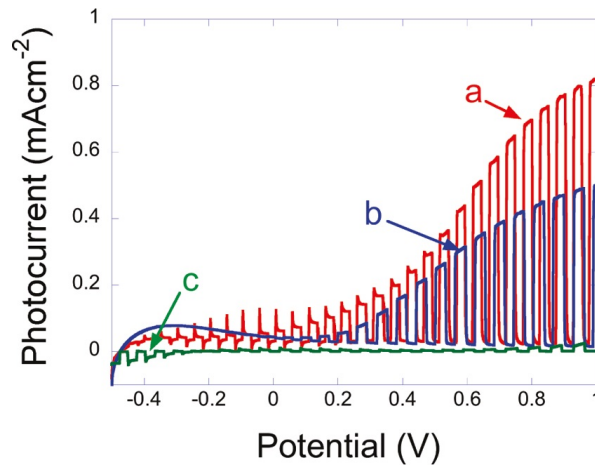


Figure 3.11: Current potential (with respect to normal hydrogen electrode NHE scale) plots for (red line, a) planar $WO_3/BiVO_4$ heterojunction film, (blue line, b) planar WO_3 film, and (green line, c) planar $BiVO_4$ film illuminated with chopped white light ($100mW/cm^2$) in an aqueous solution of $0.5mol \cdot L^{-1}$ sodium sulfate (Na_2SO_4) [6].

3.10 Catalyst: Mixed cobalt iron compounds

Even if the valence bands are ideally aligned, large additional positive applied potentials are still required to access high photon-to-current conversion efficiencies. In order to reduce this necessity of strong positive bias, it is usually deposited an electrocatalyst on the surface of the photoanode to act as a co-catalyst. This strategy is often suc-

cessful, yielding enhanced photocurrents and reduced water oxidation onset potentials. $CoFe - PB$ is an effective and inexpensive electrocatalyst. In fact it shows exceptional stability, even in acidic media, and low water oxidation onset potentials. PB, also said Prussian blu, whose formal name is iron(III) hexacyanoferrate(II) and has the chemical formula $Fe_4[Fe(CN)_6]_3$. Fig. 3.12 shows its unit cell, which has a cubic lattice structure. It has recently been demonstrated that $CoFe - PB$ modification of mesostructured

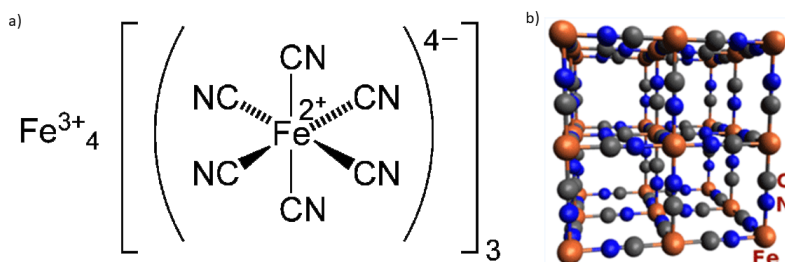


Figure 3.12: a)Structure and b) unit cell of PB.

$BiVO_4$ photoanodes produces substantial improvements in both the onset potential and photocurrent, maintaining stability for over 50 h [13]. The origin of this improvement is related to more efficient hole transfer to water, presumably via $CoFe - PB$; this is also consistent with hybrid density functional theory calculations, that predict the existence of a strong energetic offset (thermodynamic driving force) for hole transfer between the valence band of $BiVO_4$ and $CoFe - PB$. Fig 3.13 a) shows that a pristine $BiVO_4$ ex-

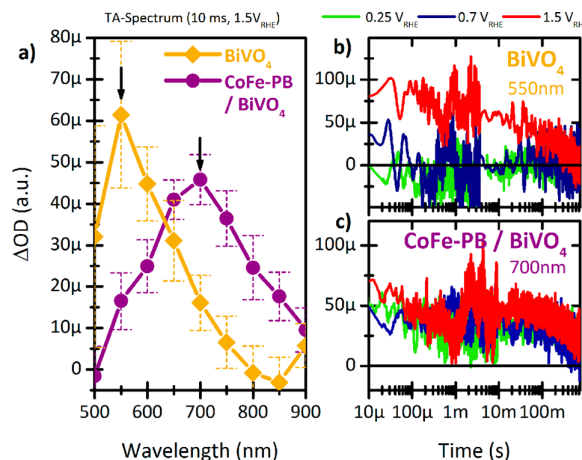


Figure 3.13: Comparison of the TA spectra of persistent photogenerated charges (recorded at 10 ms) in $CoFe - PB$ modified and unmodified $BiVO_4$ [14].

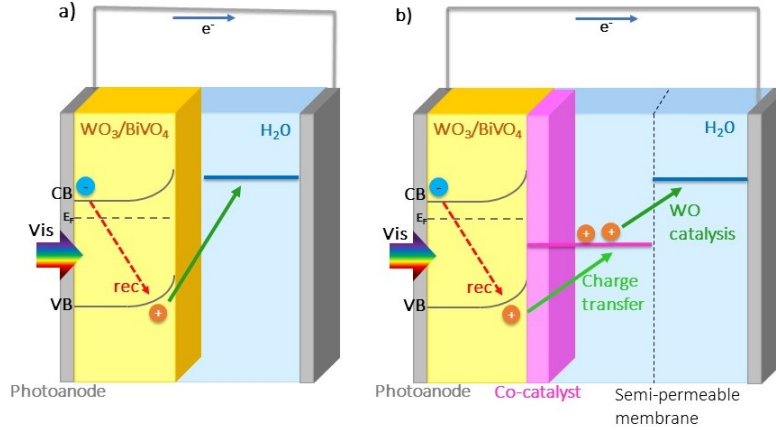


Figure 3.14: a) Processes in unmodified $WO_3/BiVO_4$, where we have the recombination competing with the water oxidation. b) Adding the catalyst $CoFePB$ the recombination current is suppressed enhancing the efficiency.

hibits a transient absorption spectrum with peaks at 550 nm and decaying toward the near-IR. After coating with $CoFe - PB$, an additional peak appears to $\sim 700\text{ nm}$, similar to the absorption of $CoFe - PB^+$. Moreover in b) is possible to notice that a persistent transient related to surface holes is observed in pristine $BiVO_4$ only at a strong positive potential ($1.5 V_{RHE}$) whereas in $CoFe - PB/BiVO_4$ a strong transient is observed at all potentials (even at $0.25 V_{RHE}$). This last section of Fig. 3.13 also shows that the signal amplitude at early times ($10\ \mu s$) is almost the same for $\sim 10\ s$. This indicates that the transfer of holes from $BiVO_4$ to $CoFe - PB$ is almost complete within the first $10\ \mu s$. This increased hole lifetime is attributed to a fast and efficient hole transfer because hole transfer to $CoFe - PB$ corresponds to a spatial separation of charge, which suppresses recombination even in the absence of a strong applied potential. This effect is shown in Fig. 3.14. This is not the only possible behaviour, in fact as explained in [15] the $CoFe - PB$ could also be an alternative pathway for water oxidation, avoiding positive charge accumulation at the $BiVO_4$ surface. Photogenerated holes can either be transferred to $CoFe - PB$ or trapped at the $BiVO_4$ surface. The transferred one will reduce the surface hole concentration, relieving to a degree the pinned quasi-Fermi level, which in turn expands the depletion region and reduces surface electron-hole recombination at less positive potentials.

Similar behaviour can also be found for *CoFeOx*, as explained in [17]. In fact a thin layer of *CoFeOx* does not affect strongly the recombination but accelerates the charge transfer as it works as a more efficient transport for holes, improving the OER charge transfer kinetics .Whereas when the thickness is higher, both the charge transfer and especially surface recombination slow down. In general, assuming that *CoFeOx* cover completely the *BiVO₄*, the photogenerated holes mainly goes to the catalyst

Chapter 4

Experimental apparatus

In this chapter, I will describe the set up and procedure used in order to perform the measurements on the samples. The goal was to collect data from X-ray absorption spectroscopy in both static and *operando* conditions. In order to do so, the set up in Fig. 4.1 was used. It is composed by:

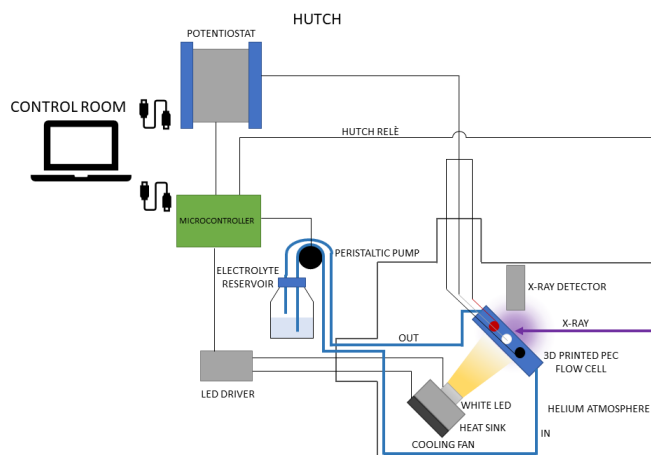


Figure 4.1: Simplified scheme of the setup for photoelectrochemical measurements.

- X-ray source
- X-ray detector
- microcontroller

- PEC cell
- potentiostat
- LED source
- peristaltic pump connected to an electrolyte reservoir

4.1 X-ray source: European Synchrotron Radiation Facility

Electrons traveling at a speed close to c , the speed of light, and forced to change the direction of their motion under the effect of magnetic fields (perpendicular to the direction of their motion), emit light known as synchrotron radiation. This feature was exploited by creating high energy electron or positron accelerators. They consist in circular system where the electrons are forced to follow the circular path under the action of magnets placed along the circumference (bending magnets). The electrons enter the storage ring only after they have been accelerated by a linear accelerator or ‘*linac*’ until their energy reaches several millions of electron volts (MeV) and then by a booster ring that gives them a boost in energy from millions to billions or giga electron volts (GeV); at that point they are transferred to the final circular accelerator as shown in Fig. 4.2.

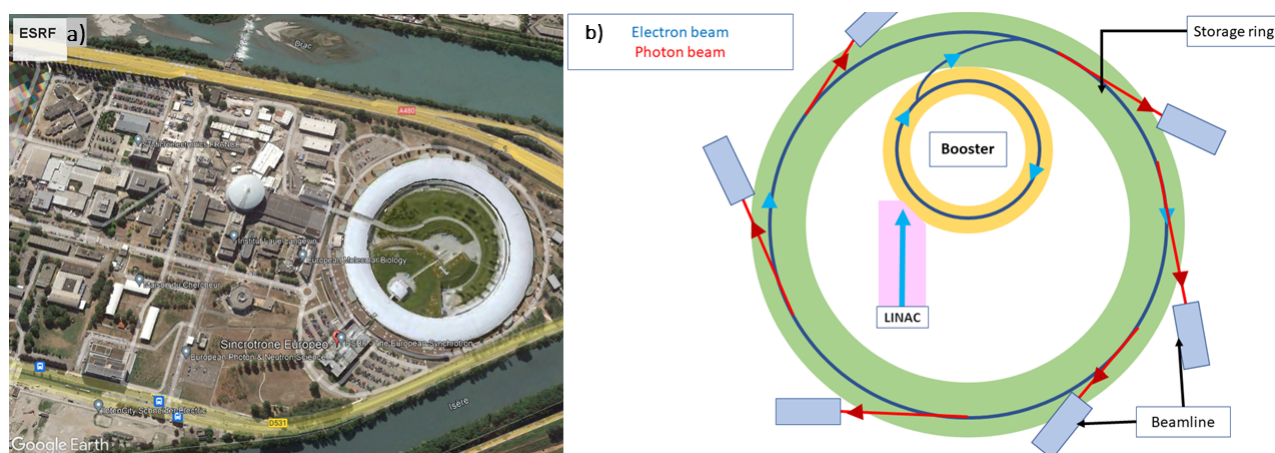


Figure 4.2: a) Satellite image of ESRF, *Earth data 2016 Google*. b) Scheme of the structure of a synchrotron. It includes a LINAC (Linear particle accelerator), a booster, a storage ring and beamlines.

The synchrotron chosen to perform our experiment was the one found in Grenoble, France, called European Synchrotron Radiation Facility (ESRF). It has:

- Energy of 6.03 GeV
- Horizontal emittance of about 3 nm rad
- Beam current of 200 mA
- Synchrotron frequency 2.10 kHz

Moreover it has 844 m circumference ring and 32 cells. After the latest improvement of the synchrotron (called EBS, extremely brilliant source) each cell is 27 m long and contain 14 vacuum chambers, 31 magnets, 10 compensating magnets and 10 beam position monitors.

4.1.1 LISA (*Linea Italiana per la Spettroscopia di Assorbimento X*) beamline

Our experiment took place in LISA [Linea Italiana per la Spettroscopia di Assorbimento X (Italian beamline for X-ray Absorption Spectroscopy)], the Italian Collaborating Research Group beamline operative at the European Synchrotron Radiation Facility. As shown in Fig. 4.3, LISA consists of three lead hutches: the optics hutch (*OH*), containing the main optical elements, the first experimental hutch (*EH1*), with the instrumentation for experiments with a non-focused beam and low-energy harmonic rejection mirrors, and finally the second experimental hutch (*EH2*), containing all the instrumentation for experiments with a focused beam. The center point of *EH2* is at 49 m from the source and it coincides with the focal point of the focusing mirror, *M2*. A 5 m long bench supports all the experimental apparata, among which there is the detector. The spectra have been collected in fluorescence mode using the *ORTEC 12-elements HP-Ge* detector mounted behind the measurement chamber and the Si(311) crystal pair. The beam was focused in a $200 \mu\text{m}$ spot and the fiber, rotated 45° with respect to the incoming X-ray beam, was oriented parallel to the radiation polarization plane, allowing a single fiber embedded in kapton to be probed.

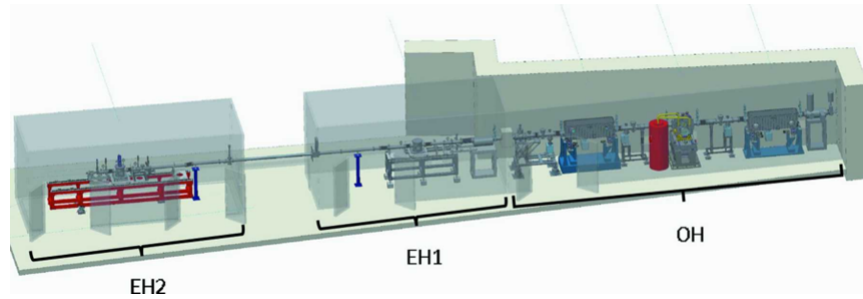


Figure 4.3: General layout of the LISA beamline. The center of the first hutch (optics hutch OH) is about 28 m from the source, the first experimental hutch ($EH1$) is at 37 m and the second experimental hutch ($EH2$) is at 49 m . [18].

$EH1$ is placed between $EH2$ and OH at 37 m from the source, here a beam spot of $\sim 1\text{ mm} \times 2\text{ mm}$ can be obtained as it is sufficiently far from the focal point of $M2$. This could be useful in case of heterogeneous samples or if the maximum flux isn't required. Finally in the optical hutch (OH) there is a vacuum vessel, which contains the principal slits and a set of attenuators (that permits the thermal load on the subsequent optical elements to be reduced). Then there is a collimating mirror $M1$, followed by the monochromator and by the focusing mirror $M2$.

4.2 The photoelectrochemical cell

The PEC cell used was designed and made inhouse. It is made by *rigid 10k resin* by Formlabs, material highly resistant to heat and chemicals. It is a three-electrode electrochemical cell with a window that allows the sample to be illuminated. Moreover, the cell was constructed to be used while the electrolyte was flowing and to avoid the formation of bubbles, that tend to create on the photoanode surface and ruin XAS measurements. The 3D sketch is shown in Fig. 4.4. One of its main component is the reservoir which is filled with the electrolyte, in which are immersed all of three electrodes. The working electrode is the sample under investigation, whose photoanodes is electrically connected to the external circuit using a copper tape and an alligator clip. The counter electrode is a platinum wire and its goal is to supply current. Instead the reference electrode, with respect to which the potential applied to the cell is measured, is made of $Ag/AgCl$ whose

$V = 0.197 \text{ mV vs NHE}$. Moreover there is a Kapton window that allows the photoanode to be immersed in the electrolyte and be illuminated at the same time.

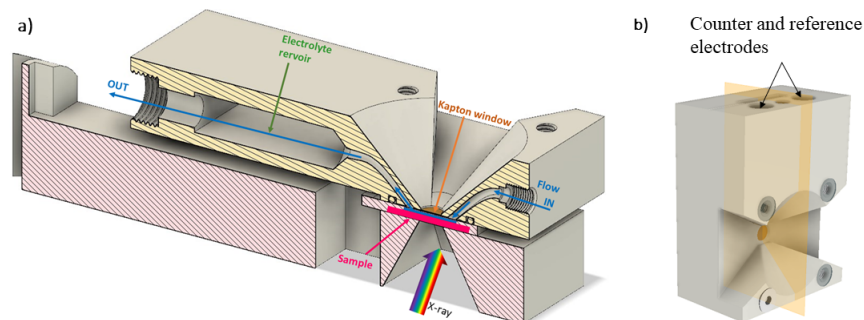


Figure 4.4: 3D sketch and pictures of the photoelectrochemical cell used for photoelectrochemical measurements. a) Cross section view. b) Complete picture of the cell from outside.

4.3 Potentiostat

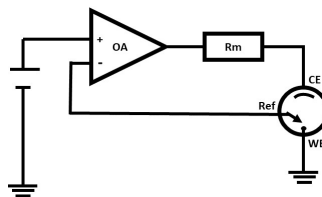


Figure 4.5: Simplified internal circuit of a potentiostat. OA is the operational amplifier that keep the voltage between the reference and the working electrode at the desired voltage.

The potentiostat is one of the most important component of the set up, in fact by using a potentiostat, the working electrode is set at a fixed potential versus the reference electrode, and the current at this potential is measured. In this type of measurement, as shown in Fig. 4.5 the counter electrode performance is not important because the potentiostat maintains the potential of the photoelectrode at the desired value and reads out the current at that potential, and it supplies whatever voltage between the photoelectrode and counter electrode is necessary in order to maintain that current.

4.4 Additional components

In order to illuminate the sample a white led source (with an incident intensity of 1 *sun*) provided with cooling fan was used. Furthermore, a peristaltic pump connected to an electrolyte reservoir was used to make the solution flow in the PEC. Both the light and the pump was controlled by LAB view software on a computer placed in the hutch. However, by using *Remmina remote desktop* we managed to control it by the control room during the measurement, as shown in Fig 4.6.

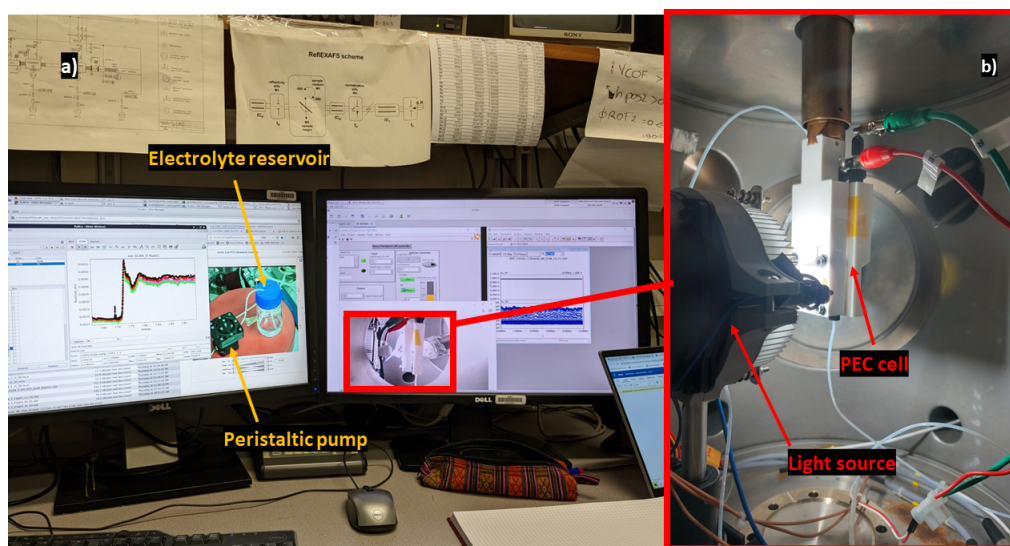


Figure 4.6: a) View of the computers in the control room while the experiment was performing. b) Inside of the chamber with light ON and PEC cell.

4.5 Data acquisition

The samples were first studied *ex-situ* (in vacuum condition) and then *in-situ* (placing Helium in the synchrotron chamber and flowing the electrolyte in the PEC cell).

Our interest is on the catalysis process as a consequence the first *operando* measurements were done while the sample was in the PEC cell submerged in an electrolyte solution borate buffer 0.5M (pH 9) connected to the electrolyte reservoir, through the peristaltic pump and biased at -0.2 V , 0.2 V and 1 V . Successively the solution was removed and

another *ex-situ* measurement was executed on both samples to observe how and if the samples were changed.

Then, to study the effect of light, we perform another *operando* XAS analog to the previous with the addition of a white led source pointing to the window of the PEC cell. Two acquisition methods were employed to investigate the effect of the light on the photoanode spectroscopical features: firstly we recorded two spectra for each of the sample, one completely in dark and the other one completely with light (the behaviour of the light is graphed in Fig. 4.7 a). Then, after improving the system, we performed another type of *operando* XAS; illuminating for 10 s and then switching OFF the light for 10 s (with a delay of 1 s) for every X-ray's energy (4.7 b).

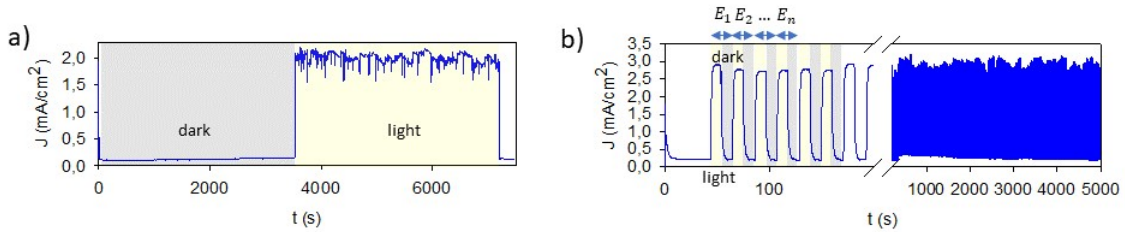


Figure 4.7: Behaviour of light during a) the first *operando* measurement with light, keeping the light always ON or OFF, and b) the second *operando* measurement, with light ON for 10 s and then OFF 10 s with a delay of 1 s for every X-ray's energy.

Finally we performed Fixed-energy X-ray absorption voltammetry (FEXRAV). It consists of recording the X-ray absorption coefficient μ at a fixed energy while varying the electrode potential and the sample is in the PEC cell with electrolyte solution borate buffer 0.5 M (pH 9). The energy is usually chosen on the edge of the spectra of the sample to give the maximum contrast between different oxidation states of the given element.

Chapter 5

Results and discussion

In this chapter I will present and discuss the obtained data using both the samples *CoFePB* and *CoFeOx*. The two samples were studied, as explained in details in 4.5, with X-ray absorption spectroscopy both in static and *operando* conditions.

5.1 Description of the samples

Both samples are made of a catalyst (*CoFeOx* or *CoFe-PB*) deposited on photoanode a $WO_3/BiVO_4$ (same for both). This was constructed in the following procedure:

1. Firstly, in order to layer WO_3 on FTO glass, a colloidal WO_3 was prepared . This was done by precipitating a C gel, adding concentrated HCl to aqueous Na_2WO_4 . Then several washings of H_2WO_4 were performed by redispersion/centrifugation and a stable H_2WO_4 sol was generated by peptization with oxalic acid (Alfa Aesar > 99.5%) at 60 °C. The obtained colloidal suspension was densified by adding 20% Carbowax (Sigma-Aldrich) and a few drops of Triton X-100 (Fluka), to improve the colloid spreadability during the subsequent FTO-coating process. Finally dry nanoparticulate films (colloidal photoanodes) were obtained onto the well-cleaned FTO glass (Pilkington TEC 7) by spin coating the H_2WO_4 aqueous colloidal precursor already described. In this particular case six layers of WO_3 were sequentially deposited, each layer being thermally annealed at 550°C for 30 min in air before

depositing the next one. At the end the total thickness of the electrode was 1 μm .

2. Subsequently, in order to deposit $BiVO_4$ on the FTO/WO_3 a previously published procedure was followed ([20]). To sum up 10 mM of $Bi(NO_3)_3$ (Sigma Aldrich > 99%) was slowly added to an acidic solution of 10 mM $VOSO_4$ (Alfa Aesar, > 99%). To dissolve completely $Bi(NO_3)_3$ dropwise concentrated HNO_3 was added, over a time of 30 min. After, by using CH_3COONa (Alfa Aesar > 99%) the pH increased to 4.5. At this point applying 210 mV between FTO/WO_3 and a platinum foil at room temperature for 300 s the solution was able to work as an electrolyte for two-electrode potentiostatic electrodeposition. Typically the distance between the FTO/WO_3 working electrode and the Pt foil was 3 mm . After deposition, the resulting FTO supported photoanode was abundantly rinsed with water, dried at room temperature, and finally annealed at 500 $^{\circ}C$ in air for 2 h .

After the preparation of the photoanode, the catalyst was ready to be deposited and, as already said, could be $CoFeOx$ or $CoFe - PB$.

5.1.1 $WO_3/BiVO_4/CoFe - PB$

To deposit Cobalt-iron Prussian blue catalyst ($CoFe - PB$) was used surface ionic layer adsorption and reaction (SILAR) at room temperature . Each deposition run was performed as follows: the $FTO/WO_3/BiVO_4$ electrode was bathed in a 0.02M $K_3[Fe(CN)_6]$ (Riedel de Haen > 99%) solution for (10 – 15) min while gently magnetically stirring the solution, following the electrode was rinsed with water and immersed in 0.04 M $CoCl_2$ (Carlo Erba > 99%) for other (10 – 15) min under stirring. This sequence was repeated for four times after washing out the $Co(II)$ excess. Finally the resulting $FTO/WO_3/BiVO_4/CoFe-PB$ electrodes were blown dried with warm air and stored in the dark at room temperature before use.

This sample was characterized by scanning electron microscopy (SEM) and X-ray Diffraction (XRD). The results, Fig. 5.1, show clearly that the colloidal WO_3 is characterized by a nanostructured morphology made of aggregated nanoparticles with an average

diameter of $(45 \pm 12) \text{ nm}$ kept together in a porous 3D network. After depositing BiVO_4 on it, a homogeneous thin layer is prepared and increases the average size of the nanoparticles to $(52 \pm 8) \text{ nm}$. The final deposition of the catalyst $\text{CoFe} - \text{PB}$ ends up in an homogeneous coating on top of BiVO_4 . Whereas the XRD shows that WO_3 films exhibit a monoclinic structure, while BiVO_4 shows the typical monoclinic clinobisvanite structure. As expected, WO_3 peak intensities are the same in all the photoanodes while the ones associated to BiVO_4 are lower in intensity due to the different thicknesses of the two layers. Finally, as expected for a very thin overlayer, the addition of the catalyst does not modify the XRD pattern.

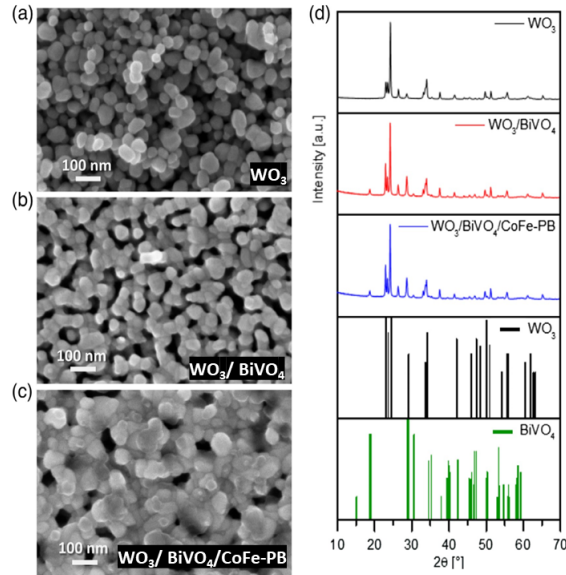


Figure 5.1: FESEM micrograph of a) WO_3 , b) $\text{WO}_3/\text{BiVO}_4$ and c) $\text{WO}_3/\text{BiVO}_4/\text{CoFe} - \text{PB}$. d) XRD pattern of the built photoanodes and the reference patterns for WO_3 and BiVO_4 [23].

Then the sample was tested electrically by performing a linear sweep voltammetry (LSV). This was performed in acetate buffer solution under chopped and static white LED illumination with an incident of 1 sun. The resulting graph is shown in Fig. 5.2 a), where is shown not only the dependence of the current on voltage but also the effect of the co-catalyst $\text{CoFe} - \text{PB}$ on the efficiency of the cell. As expected, from 3.10, the photocurrent of the PEC cell with the cocatalyst is higher for potential range $(0 - 1) \text{ V}$

and starts at lower potential.

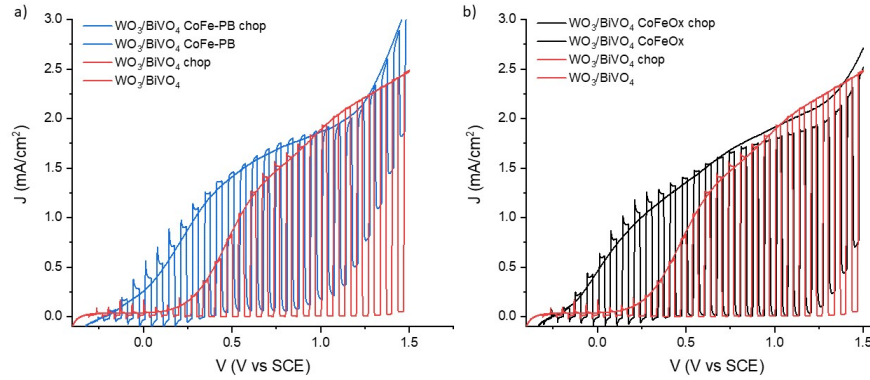


Figure 5.2: Linear sweep voltammetry under 1-sun equivalent illumination in acetate buffer solution (pH 5) of only $WO_3/BiVO_4$ (red line) and in presence of the co-catalyst a) $CoFePB$ (blue line); b) $CoFeOx$ (black line).

5.1.2 $WO_3/BiVO_4/CoFeOx$

Whereas cobalt–iron (oxy)hydroxide catalyst, ($CoFeOx$) was prepared by doing an electrodeposition bath with 16 mM of $CoCl_2$, 5 mM of $Fe_2(SO_4)_3$, Millipore deionized water (18.2 $M\Omega cm$) and 0.1 M $NaOAc$ (as a supporting electrolyte). The solution have a pH of ~ 5.3 . Then, to electrodeposit, 10 consecutive linear sweeps was performed by applying a voltage (1.35 – 1.65) V_{RHE} , obtaining a layer of width 1 nm. The sample was then tested electrically by performing LSV, obtaining the result in Fig. 5.2 b). As expected it is possible to see that in presence of the catalyst the on-set potential is smaller and the photocurrent is higher for $V_{RHE} < 1V$.

5.2 *Ex-situ* XAS investigation

The samples were then studied using X-ray absorption spectroscopy to study the atomic and electronic configuration. As already explained in 4.5 they were first studied *ex-situ* (in vacuum condition) and then *in-situ* (placing Helium in the synchrotron chamber)

In Fig. 5.3 we report the Fe K-edge XANES spectra for the two catalysts. The spectra

were processed using *Athena* software and setting E_0 as 7123.35 eV and 7125.91 eV for respectively *CoFeOx* and *CoFe - PB*. *Athena* is useful to observe better the spectra as it regresses a line in the pre edge and normalization range. Both the ranges are defined by the users and the post-edge line is usually a three-term (quadratic) polynomial. Fig. 5.3 a) shows the resulting spectra. Both samples show a weak pre-edge absorption feature (A) at 7113 eV, followed by the main absorption edge (B) at 7129 eV for *CoFeOx*, and 7131 eV for *CoFe - PB*. The main peak (B) is a consequence of a dipole-allowed $1s - 4p$ transition whereas the pre-edge feature just below the threshold is mainly due to a $1s - 3d$ quadrupole transition.

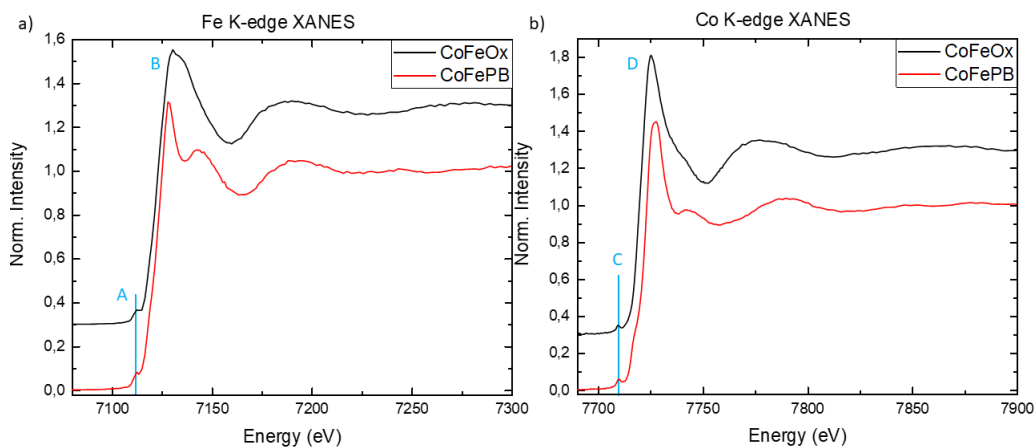


Figure 5.3: a) Fe K-edge and b) Co K-edge spectra performed on *CoFeOx*, black line, and *CoFe - PB*, red line. The spectra of *CoFeOx*, black line, was shifted on the y-axis by a value of 0.3 to show better both the spectra.

In Fig. 5.3 b) we report also the Co K-edge XANES spectra for the two catalysts after being plotted with *Athena* and set E_0 as 7721.76 eV and 7723.75 eV for *CoFeOx* and *CoFe - PB*. The spectra is characterized by a low intensity peak at 7709 eV (C) and the main absorption edge 7725 eV for *CoFeOx* and 7727 eV for *CoFe - PB* (D). As for the Fe K-edge spectra the pre-edge with weak intensity corresponds to the $1s - 3d$ absorption process whereas the main one to the $1s - 4p$ transition [22].

Finally, in order to perform an EXAFS study the spectra were reported as a function of the photo-electron wave vector k . In Fig. 5.4 is showed *CoFe - PB* and *CoFeOx* EXAFS spectra and their Fourier Transformation (FT). In the FT is possible to see multiple

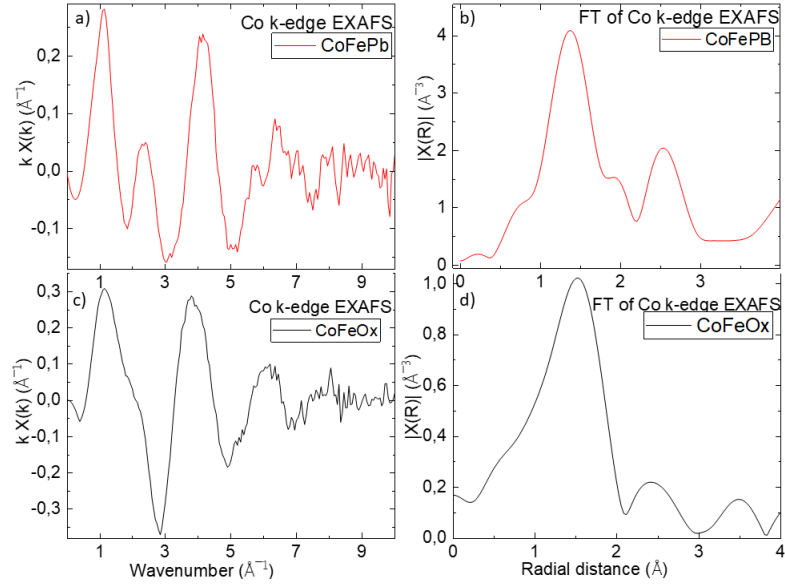


Figure 5.4: Co k-edge EXAFS spectra and its Fourier of *CoFe – PB* a)-b) and *CoFeOx* c)-d).

peaks, which correspond both to single or multiple scattering of atoms. The first and most prominent peaks which are due to single or multiple scattering contributions related to the atoms in the first few coordination shells. In order to understand better the origin

Table 5.1: Setting used to perform the fitting of the Co k-edge spectra with *FeCo(CN)₆* on *Artemis* software. Where $R_{eff} + \Delta R$ is the expected path plus a correction, degeneracy is the coordination number and Debye-Waller Factor accounts for the mean square variation in path length due to thermal or structural disorder. Moreover the k-range was chosen as $(3 - 9.86) \text{ \AA}^{-1}$.

Path	$R_{eff} + \Delta R$ (Å)	Degen.	Debye-W.factor (Å ²)
N	1.954 ± 0.027	6	0.01102 ± 0.0048
C	3.034 ± 0.23	6	0 ± 0.079
N-C	2.97 ± 0.11	12	0.014 ± 0.027
N-C-N	3.036 ± 0.504	6	0.0013 ± 0.039
N	3.69 ± 0.79	6	0.013 ± 0.085

of this peaks we used *Artemis* software. It enables to compare the Fourier transform of our sample with the one of a known structure (choosing the paths that we want to include). By including the paths in Table 5.1 of the known structure *COFe(CN)₆* (using the .cif file) we got Fig. 5.5. Here is possible to understand that the first and highest peak is due

to Nitrogen. whereas the second one is due to both the single scattering of Carbon and the multiple one of Carbon and Nitrogen.

Unfortunately the structure of $CoFeOx$, as shown in Fig. 5.4 d) is too messy to be interpreted and compared with a known structure in Artemis software.

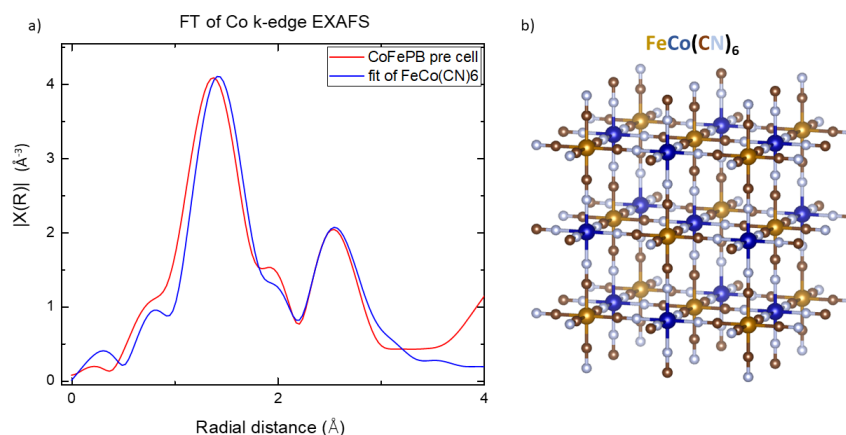


Figure 5.5: a) FT of Co k-edge EXAFS of $COFe - PB$ (red line) and the reference one of $FeCo(CN)_6$ (blue line). b) Structure of molecule $FeCo(CN)_6$.

5.3 Operando XAS investigation

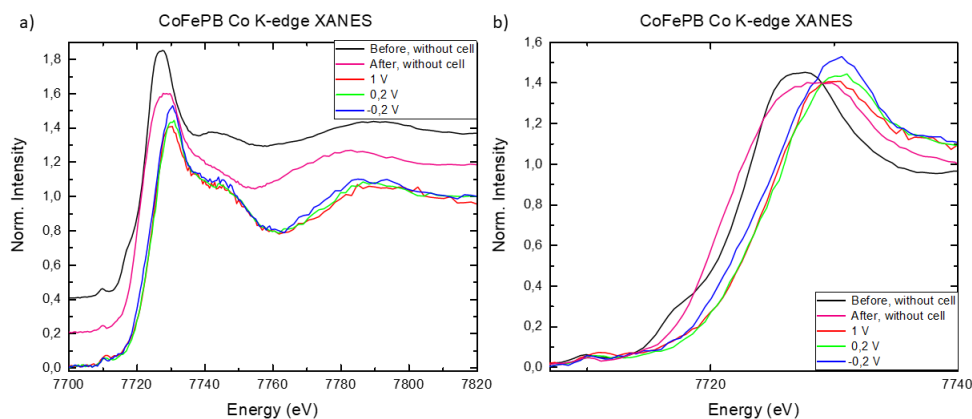


Figure 5.6: a) Co k-edge XANES of $COFe - PB$ while the sample was in the PEC cell with electrolyte solution borate buffer 0.5 M ($pH9$), biased at various voltages. The spectra taken before and after (black and pink lines) was taken *ex-situ* and shifted on the y-axis to show better the features of interest. b) Enlargement of the edge region to observe better the shift.

After investigating the samples *ex-situ*, we placed one sample at a time in the PEC cell with an electrolyte solution borate buffer 0.5 M (pH 9) and biased at -0.2 V, 0.2 V and 1 V. Differently from the *ex-situ* case, here the chamber was filled with Helium. For every voltage we measure a XAS spectra and by plotting all of these together we obtain Fig. 5.6 for *CoFe – PB* and 5.7 for *CoFeOx*. Here is possible to notice that in both samples the biggest edge shifts happens when the sample is in the PEC cell with electrolyte and under applied bias. In fact it shifts to higher energies, which means they oxidize.

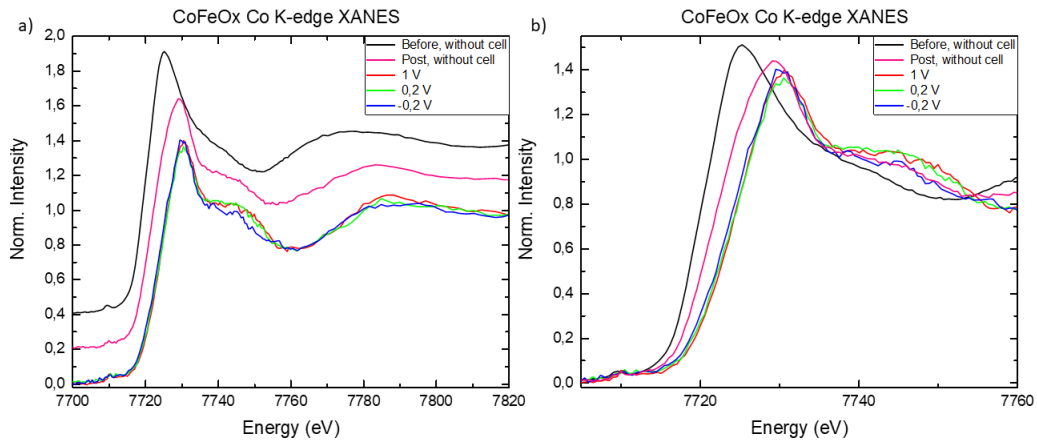


Figure 5.7: a) Co k-edge XANES of *CoFeOx* while the sample was in the PEC cell with electrolyte solution borate buffer 0.5 M (pH9), biased at various voltages. The spectra taken before and after (black and pink lines) was taken *ex-situ* and shifted on the y-axis to show better the features of interest. b) Enlargement of the edge region to observe better the shift.

To better appreciate the behavior, in Fig 5.8 is shown the difference between the spectra using the 0.2 V one as a reference. For both samples, the spectra are substantially overlapped between 0.2 V and 1 V, suggesting that the oxidation state in this potential range is stable. On the other hand, a larger difference is noticed at -0.2 V, where the increased μ in the edge region suggests a red-shift of the absorption edge, compatible to a reduction process. Therefore, in order to understand the process happening I looked for known oxidized compound of Cobalt with a similar spectra. The XANES spectra of *CoFe – PB*, in *operando* conditions, is compatible with the one exhibited by a Co-oxo cubane, prepared upon oxidative polarization of indium tin oxide (*InSnO₃*) in a

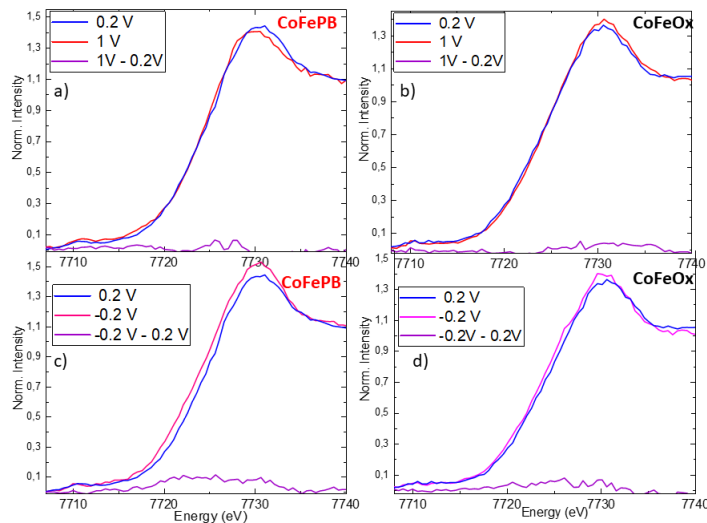


Figure 5.8: Comparison of Co K-edge XANES of *CoFe – PB* a)-c) and *CoFeOx* b)-d) while the sample was in the PEC cell with electrolyte solution borate buffer $0.5M$ (pH 9), biased at various V . The voltage $0.2 V$ (blue line) was used as reference and the difference between the spectra is always plotted as the purple line.

phosphate (Pi) buffer from reactant Co^{2+} ions in aqueous solution, hereby called CoCat. It has an oxidation state of $\sim 3^+$ and from the spectral shape of the Co XANES region we understand that it has a near-octahedral coordination of Co by six oxygen ligands (CoO_6) [26]. This means that *CoFe – PB* degrades into a similar compound upon exposure to the electrolyte.

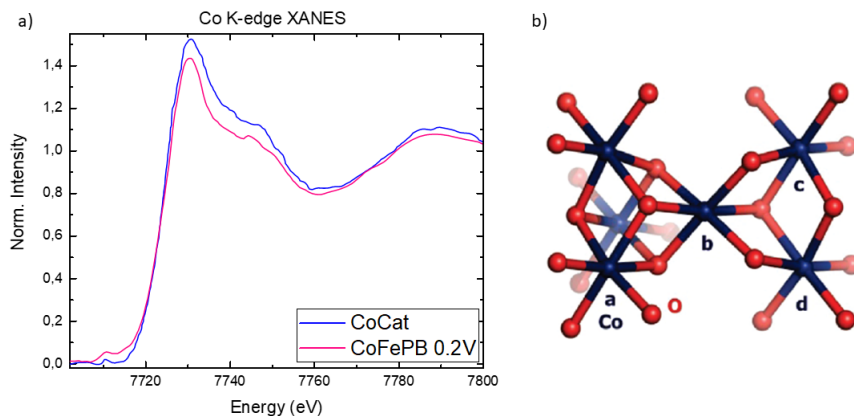


Figure 5.9: a) Comparison of Co k-edge XANES of *CoFe – PB* in *operando* conditions and the reference spectra of CoCat. b) CoCat's structure [26].

After performing *in-situ* measurements at various voltages, the solution was removed

and it was executed an *ex-situ* measurement on both sample to observe how and if the samples were changed. In Fig. 5.6 and 5.7 the pink line shows the XANES of the samples after the photoelectrochemical process. From these is possible to see that even if both $CoFe - PB$ and $CoFeOx$ get oxidized when in the PEC cell with applied V, once the solution is removed they tend to revert to the initial state, reducing.

Successively to understand the effect of light on the catalysts, measurements were done while enlightening the samples constantly (static measurements). Fig. 5.10 shows the resulting spectra for $CoFe - PB$ and is possible to notice that spectra with light ON and OFF have same edge and shape. However is possible to see a positive difference between ON and OFF at 0.2 V in the range (7720 – 7750) eV.

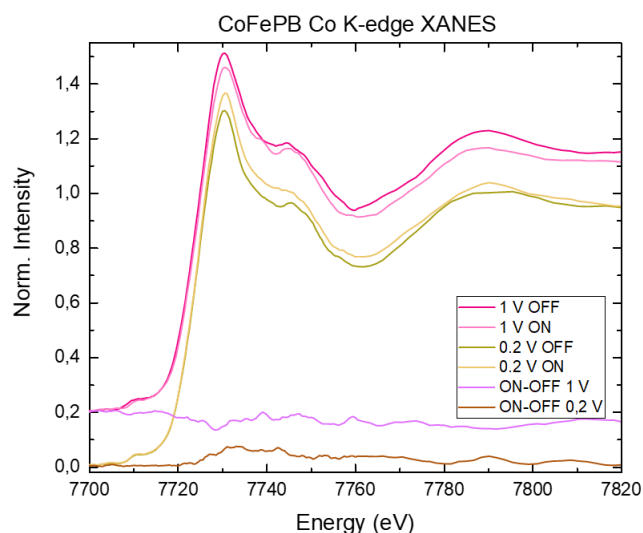


Figure 5.10: Co K-edge XANES of $CoFe - PB$ while the sample was in the PEC cell with an electrolyte solution borate buffer 0.5 M (pH 9) and biased at various voltages with light OFF or ON. The light purple and brown line show the difference between the ON and OFF spectra at the same V.

Then after improving the system set up, a different type of *operando* measurement was done for both $CoFe - PB$ and $CoFeOx$. For every X-ray's energy one measurement was performed in light and one in dark. This was possible by turning the light ON for 10 s and then OFF 10 s (with a delay of 1 s) for every X-ray's energy (dynamic measurements). Fig. 5.11 shows the resultant spectra. First of all is important to notice that for all the

bias applied there is no difference between the spectra with light ON and OFF except for *CoFe – PB* biased at 0.2 V in the range (7724 – 7736) eV, which was found also in the static light case.

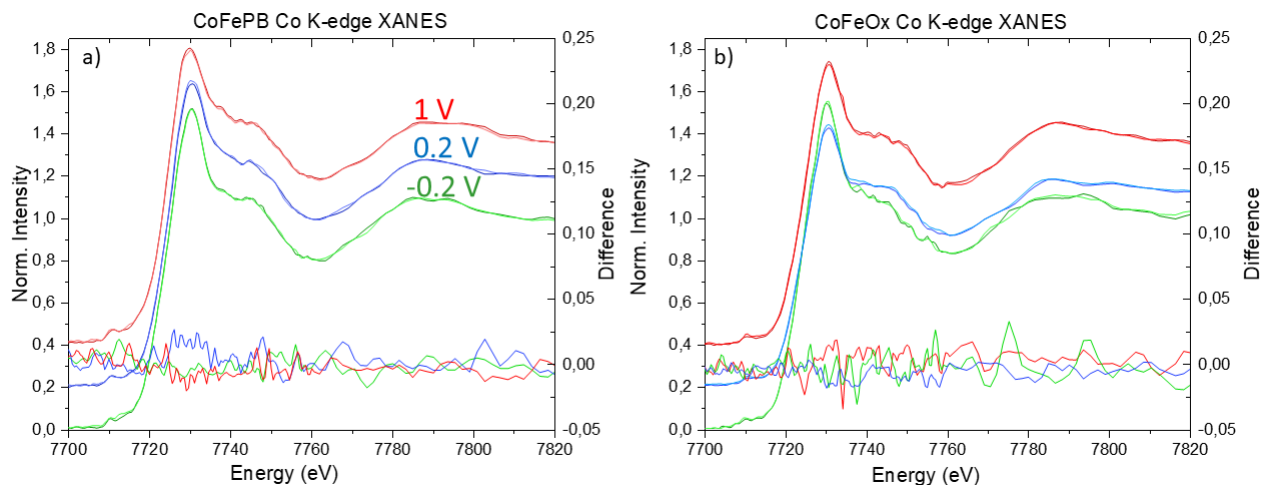


Figure 5.11: Co k-edge XANES of a) *CoFe – PB* and b) of *CoFeOx* while the sample was in the PEC cell switching light OFF 10 s then ON for 10 s (with delay of 1 s) while the sample was immersed in an electrolyte solution borate buffer 0.5 M (pH 9) and biased at various voltages.

5.4 FEXRAV: Fixed energy X-ray absorption voltammetry

Finally, fixed-energy X-ray absorption voltammetry (FEXRAV) was performed. As said in 4.5, it consists of recording the X-ray absorption coefficient μ at a fixed energy while varying the electrode potential and the sample is in the PEC cell with electrolyte. The energy was fixed on the maximum derivative of the spectra of the sample while in solution in order to give the maximum contrast between different oxidation states of a given element. Fig. 5.12 a) shows the FEXRAV of *CoFe – PB*, performed at energy 7722.5 eV. Moreover, in the same graph is possible to see that both in dark and light μ is the highest at the lowest voltage (and current); Instead, at the maximum voltage the absorption coeff. is the minimum. Therefore, the maximum value of μ , that could correspond to a reduced state of *CoFe – PB*, is obtained for $V = -0.2$ V. This is also confirmed by the *operando* spectra in Fig 5.6 where the blue line, the one of -0.2 V, is

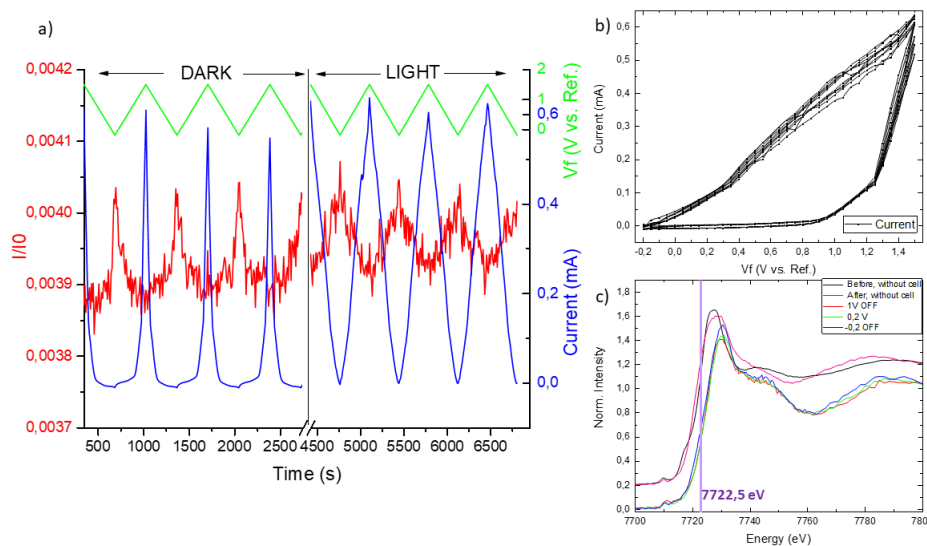


Figure 5.12: a) Co k-edge FEXRAV of *CoFe-PB*, with an applied voltage $[(-0.2) - (1.5)]$ V and energy fixed at 7722.5 eV. In the graph is shown the μ (red line), the current (blue line), and the voltage (green line) as a function of time. b) Cyclic voltammetry of *CoFe-PB* in the range -0.2 V $< V$ vs Ref. < 1.5 V. c) Co k-edge spectra of *CoFe-PB* with a light purple line on 7722.5 eV, the energy chosen to perform FEXRAV.

red shifted compared to the one of 0.2 V (green line) and 1 V (red line). It is interesting to notice that in absence of light excitation of the semiconductor/co-catalyst interface, a slow increase of μ is observed upon sweeping the potential from 1.5 V to 0.05 V, while a faster rise is visible when approaching -0.2 V. The potential range, where increased μ can be appreciated, is strongly widened upon illumination of the sample, meaning that less negative potentials are needed to promote the reduction process.

Fig 5.13 shows instead the FEXRAV for *CoFeOx* sample at energy 7719.5 eV. Also here is possible to see that the maximum of μ is obtained for the minimum of V which is -0.2 V, confirmed in Fig. 5.7. During the first potential sweeps in absence of light, the average absorption coefficient seems to decrease, presumably due to slight photocorrosion, later stabilizing to more constant values. More importantly, the intensity peak is now broader suggesting a less thermodynamically demanding reduction process. Conversely, the peak width shrinks upon illumination, unlike what happens in *CoFe-PB*, where the opposite trend is observed. Therefore in the *CoFeOx* case it takes an higher voltage in light than in dark to start the oxidation process.

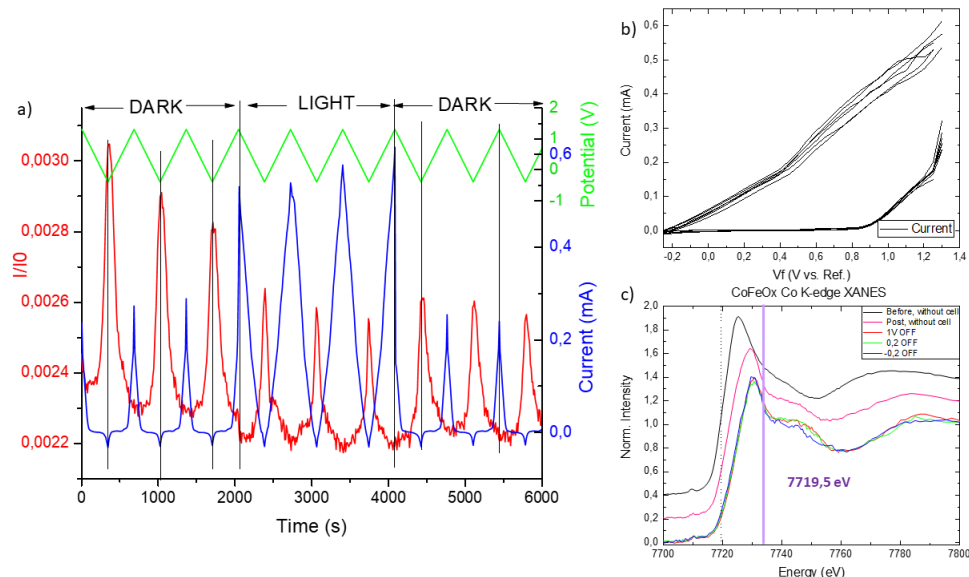


Figure 5.13: a) Co k-edge FEXRAV of $CoFeOx$, with an applied voltage $[(-0.2) - (1.5)] V$ and energy fixed at $7719.5 eV$. In the graph is shown the μ (red line), the current (blue line), and the voltage (green line) as a function of time. b) Cyclic voltammetry of $CoFeOx$ in the range $-0.2 V < V vs Ref < 1.5 V$. c) Co k-edge spectra of $CoFeOx$ with a light purple line on $7719.5 eV$, the energy chosen to perform FEXRAV.

A possible explanation of this phenomenon could be related to the transfer of charge between $BiVO_4$ and the co-catalyst.

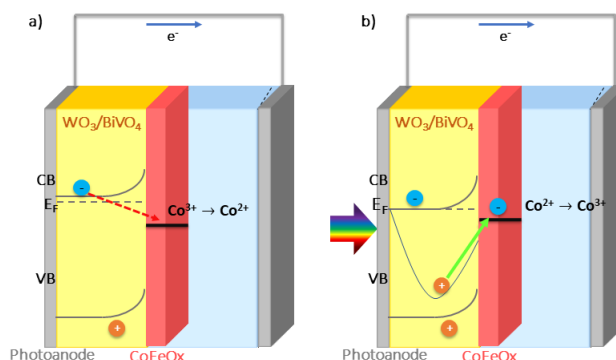


Figure 5.14: PEC cell using $CoFeOx$ as cocatalyst a) in dark and b) illuminated. The cocatalyst is first reduced in dark and then, oxidized in light due to the quasi-Fermi level at more positive energy.

In fact, as explained in Fig. 5.14 a), $CoFeOx$ is reduced at lower potential when there is no light, this could mean that the Fermi energy of $BiVO_4$ is higher than the one of the catalyst, therefore the e^- goes from the photoanodes to the catalyst, reducing it. When

the sample is illuminated, Fig. 5.14 b), the quasi-Fermi level becomes more positive and the photogenerated holes have no other pathways but recombination with the electrons of the catalyst (that was previously reduced).

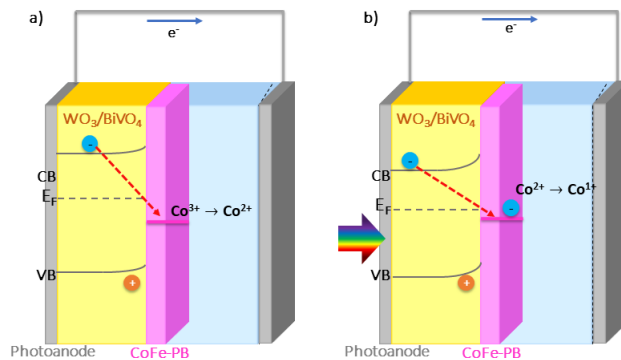


Figure 5.15: PEC cell using $CoFe - PB$ as cocatalyst a) in dark and b) illuminated. The cocatalyst is reduced in dark and then a second time in light due to the Fermi level at more negative energy in both cases and a small band bending.

Unexpectedly the same process does not happen for $CoFe - PB$, here in fact reduction peak widens upon illumination, pointing out that there is not a photo-oxidation current opposite to the first reduction one, Fig 5.15 b). A possible explanation to this phenomenon may be related to a more negative reduction potential for the $Co^{III} - Co^{II}$ couple in $CoFe - PB$, highlighted by the smaller potential region of the intensity peak. The spontaneous charge transfer between $BiVO_4$ and $CoFe - PB$ occurring upon coupling the two materials in the heterostructure, may be thus limited. Upon illumination, as the lower charge equilibration suggests lower band bending, photoreduction of the cobalt center may take place, widening the potential region for the process. Despite the efforts to model the differences between co-catalyst, further investigation is required to achieve a better understanding of the physics underlying the process.

Chapter 6

Conclusions

In this thesis X-ray absorption spectroscopy (XAS) was used to study the local atomic and electronic structure of the samples. Moreover by applying a bias and turning on a light on the samples during the measurements we were able to study local structure around these cations in static and *operando* conditions. Firstly *ex-situ* XAS measurements were performed on the samples $WO_3/BiVO_4/CoFe - PB$ and $WO_3/BiVO_4/CoFeOx$, analyzing both the XANES and EXAFS spectra and comparing through *Artemis* software the Fourier transform of $CoFe - PB$ spectra and the reference one of $FeCo(CN)_6$. Then, the samples were placed in the photoelectrochemical cell (specifically designed during my thesis to do this experiment) and biased at various voltages, figuring out that both the co-catalyst oxidize while in the PEC cell. Moreover the spectra of $CoFe - PB$, while in the PEC, is compared to the one of CoCat(Co-oxo cubane prepared upon oxidative polarization of indium tin oxide ($InSnO_3$) in a phosphate (*Pi*) buffer from reactant Co^{2+} ions in aqueous solution). Successively the electrolyte was removed and the samples were studied again in *ex-situ* condition finding out that after the photoelectrochemical process the samples tend to revert to the initial state.

Then, to study the effect of light we performed two different type of *operando* measurements, while the samples were in the PEC cell with electrolyte. Firstly by illuminating constantly and, after improving the system, by enlightening intermittently the sample.

From both the techniques it is possible to observe that ON and OFF spectra have same edge and shape even if, paying more attention, there is a positive difference in the range (7720 – 7740) eV for the applied bias of 0.2 V . Finally, we performed FEXRAV (fixed energy X-ray absorption voltammetry) choosing as energy the maximum derivative of the spectra while the sample was in solution and as voltage range $[(-0.2) - (1.5)] V$. Here it is possible to notice that the two samples have different behaviour. In fact for $CoFe - PB$ it takes an higher voltage in dark than in the light to start the oxidation process whereas for $CoFeOx$ is the opposite. This could be due to different recombination of electrons between the co-catalyst and $BiVO_4$.

Bibliography

- [1] P. Breeze, Solar power, in: *Power Generation Technologies*, third ed., Elsevier, Feb. 2019, pp. 293–321 (Chapter 13).
- [2] "Introduction to X-Ray Absorption Spectroscopy", S. Mobilio, F. Boscherini, C. Meneghini, "Synchrotron Radiation", 2015, Springer
- [3] R. van de Krol, M. Grätzel, "Photoelectrochemical Hydrogen Production", 2012, Springer
- [4] *ACS Appl. Mater. Interfaces* 2017, 9, 23, 19780–19790.
- [5] *Energy Fuels* 2022, 36, 11404-11427.
- [6] *Nano Lett.* 2011, 11, 5, 1928–1933 Publication Date: April 22, 2011.
- [7] J. Reichman, "The current-voltage characteristics of semiconductor-electrolyte junction photovoltaic cells", *Appl. Phys. Lett.* 36 (1980) 574-577.
- [8] S. Hilliard, "Water splitting photoelectrocatalysis : the conception and construction of a photoelectrocatalytic water splitting cell. Material chemistry", 2016. English. NNT : 2016PA066034.
- [9] *J. Chem. Educ.* 2007, 84, 4, 685
- [10] K. Sivula and R. van de Krol, *Nat. Rev. Mater.*, 2016, 1, 15010
- [11] P. Vecchi, A. Piccioni, R. Mazzaro, M. Mazzanti, V. Cristino, S. Caramori, L. Pasquini, "Charge Separation Efficiency in WO₃/BiVO₄ Photoanodes with CoFe Prussian Blue Catalyst Studied by Wavelength-Dependent Intensity-Modulated Photocurrent Spectroscopy", 2022, Solar RRL
- [12] Dias, P., Mendes, A. (2018). Hydrogen Production from Photoelectrochemical Water Splitting. In: Meyers, R. (eds) *Encyclopedia of Sustainability Science and Technology*. Springer, New York, NY.
- [13] *ACS Appl. Mater. Interfaces* 2017, 9, 37671-37681.
- [14] *ACS Energy Lett.* 2019, 4, 1, 337–342
- [15] Carroll, G. M.; Gamelin, D. R. Kinetic Analysis of Photoelectrochemical Water Oxidation by Mesostructured Co-Pi/ α -Fe₂O₃ Photoanodes. *J. Mater. Chem. A* 2016, 4 (8), 2986-2994.

- [16] Enman, L. J.; Stevens, M. B.; Dahan, M. H.; Nellist, M. R.; Toroker, M. C.; Boettcher, S. W. Operando X-Ray Absorption Spectroscopy Shows Iron Oxidation Is Concurrent with Oxygen Evolution in Cobalt–Iron (Oxy)Hydroxide Electrocatalysts. *Angew. Chemie Int. Ed.* 2018, 57 (39), 12840–12844.
- [17] Zhang, J.; García-Rodríguez, R.; Cameron, P.; Eslava, S. Role of Cobalt-Iron (Oxy)Hydroxide (CoFeOx) as Oxygen Evolution Catalyst on Hematite Photoanodes. *Energy Environ. Sci.* 2018, 11 (10), 2972–2984.
- [18] D’Acapito F, Lepore GO, Puri A, Laloni A, La Manna F, Dettona E, De Luisa A, Martin A. The LISA beamline at ESRF. *J Synchrotron Radiat.* 2019 Mar 1;26(Pt 2):551-558.
- [19] Puri, A.; Lepore, G.O.; d’Acapito, F. The New Beamline LISA at ESRF: Performances and Perspectives for Earth and Environmental Sciences. *Condens. Matter* 2019, 4, 12. <https://doi.org/10.3390/condmat4010012>
- [20] V. Cristino, L. Pasti, N. Marchetti, S. Berardi, C. A. Bignozzi, A. Molinari, F. Passabi, S. Caramori, L. Amidani, M. Orlandi, N. Bazzanella, A. Piccioni, J. Kopula Kesavan, F. Boscherini, L. Pasquini, *Photochem. Photobiol. Sci.* 2019, 18, 2150.
- [21] A. Thompson, D. Attwood, E. Gullikson, M. Howells, K.-J. Kim, J. Kirz, J. Kortright, I. Lindau, Y. Liu, P. Pianetta, A. Robinson, J. Sconfield, J. Underwood, G. Williams, H. Winick. X-RAY DATA BOOKLET, 2009, Center for X-ray Optics and Advanced Light Source, Lawrence Berkeley National Laboratory.
- [22] Vank’o, G.; Groot, F. M. F. de; Huotari, S.; Cava, R. J.; Lorenz, T.; Reuther, M. Intersite 4p-3d hybridization in cobalt oxides: a resonant x-ray emission spectroscopy study. *arXiv:0802.2744v1* 2008, 1–7.
- [23] P. Vecchi, A. Piccioni, R. Mazzaro, M. Mazzanti, V. Cristino, S. Caramori, L. Pasquini, "Charge Separation Efficiency in WO₃/BiVO₄ Photoanodes with CoFe Prussian Blue Catalyst Studied by Wavelength-Dependent Intensity-Modulated Photocurrent Spectroscopy", 2022, Solar RRL
- [24] K. Sivula, R. Zboril, F. Le Formal, R. Robert, A. Weidenkaff, J. Tucek, J. Frydrych, M. Gratzel, *J. Am. Chem. Soc.* 2010, 132, 7436– 7444.
- [25] L. A. Marusak, R. Messier, W. B. White, *J. Phys. Chem. Solids* 1980, 41, 981 –984.
- [26] *Chem. Soc. Rev.*, 2017,46, 102-125